

Properties of Cold Dark Matter Halos at $z > 6$

Renyue Cen¹, Feng Dong², Paul Bode³, and Jeremiah P. Ostriker⁴

ABSTRACT

We compute the properties of dark matter halos with mass $10^{6.5} - 10^9 M_\odot$ at redshift $z = 6 - 11$ in the standard cold dark matter cosmological model, utilizing a very high resolution N-body simulation. We find that dark matter halos in these mass and redshift ranges are significantly biased over matter with a bias factor in the range $2 - 6$. The dark matter halo mass function displays a slope of 2.05 ± 0.15 at the small mass end. We do not find a universal dark matter density profile. Instead, we find a significant dependence of the central density profile of dark matter halos on halo mass and epoch with $\alpha_0 = 0.4 - 1.0$; the high-mass ($M \geq 10^8 M_\odot$) low-redshift ($z \sim 6$) halos occupy the high end of the range and low-mass ($M \sim 10^7 M_\odot$) high-redshift ($z \sim 11$) halos occupy the low end. Additionally, for fixed mass and epoch there is a significant dispersion in α_0 due to the stochastic assembly of halos. Our results fit a relationship of the form $\alpha_0 = 0.75((1+z)/7.0)^{-1.25}(M/10^7 M_\odot)^{0.11(1+z)/7.0}$ with a dispersion about this fit of ± 0.5 and no systematic dependence of variance correlated with environment. The median spin parameter of dark matter halos is $0.03 - 0.04$ but with a large lognormal dispersion of ~ 0.4 . Various quantities are tabulated or fitted with empirical formulae.

Subject headings: cosmology: theory—intergalactic medium—large-scale structure of universe—quasars: absorption lines

¹Princeton University Observatory, Princeton University, Princeton, NJ 08544; cen@astro.princeton.edu

¹Princeton University Observatory, Princeton University, Princeton, NJ 08544; feng@astro.princeton.edu

¹Princeton University Observatory, Princeton University, Princeton, NJ 08544; bode@astro.princeton.edu

¹Princeton University Observatory, Princeton University, Princeton, NJ 08544; jpo@astro.princeton.edu; Institute for Astronomy, Cambridge University, Cambridge, England; jpo@ast.cam.ac.uk

1. Introduction

The reionization epoch is now within the direct observational reach thanks to rapid recent observational advances in two fronts — optical quasar absorption from Sloan Digital Sky Survey (SDSS) (Fan et al. 2001; Becker et al. 2001) and the Wilkinson Microwave Anisotropy Probe (WMAP) experiment (Kogut et al. 2003). The picture painted by the combined observations, perhaps not too surprisingly, strongly suggests a complex cosmological reionization process, consistent with the double reionization scenario (Cen 2003). It may be that this is the beginning of a paradigm shift in our focus on the high redshift universe: the star formation history of the early universe can now be observationally constrained.

It thus becomes urgent to theoretically explore galaxy and star formation process at high redshift in the dark age ($z \geq 6$). In the context of the standard cold dark matter model it is expected that stars within halos of mass $10^7 - 10^9 M_\odot$ at high redshift play an important, if not dominant, role in determining how and when the universe was reionized. Furthermore, these fossil halos may be seen in the local universe as satellites of giant galaxies. This linkage may potentially provide a great leverage to nail down the properties of the high redshift galaxies.

In this paper, as a step towards understanding galaxy formation at high redshift, we investigate the properties of dark matter halos at $z \geq 6$, using very high resolution TPM N-body (Bode et al. 2001; Bode & Ostriker 2003) simulations. While there is an extensive literature on properties of halos at low redshift, there is virtually no systematic study of dark halos at $z \geq 6$. The LCDM simulation has a comoving box size of $4h^{-1}\text{Mpc}$ with $512^3 = 10^{8.2}$ particles, a particle mass of $m_p = 3.6 \times 10^4 h^{-1} M_\odot$, and comoving gravitational softening length of $0.14 h^{-1}\text{kpc}$. These resolutions allow us to accurately characterize the properties of halos down to a mass $10^{6.5} h^{-1} M_\odot$ (having about 100 particles within the virial radius). The outline of this paper is as follows. The simulation details are given in §2. In §3 we quantify properties of dark matter halos in the mass range $10^{6.5} - 10^9 M_\odot$, including the mass function, bias and clustering properties, density profile distribution, angular momentum spin parameter distribution, internal angular momentum distribution and peculiar velocity distribution. We conclude in §4.

2. The Simulation

A standard spatially flat LCDM cosmology was chosen, with $\Omega_m = 0.27$ and $\Omega_\Lambda = 0.73$; the Hubble constant was taken to be 70 km/s/Mpc . The initial conditions were created using the GRAFIC2 package by Bertschinger (2001). The matter transfer function was calculated

with the included Boltzmann integrator (Ma & Bertschinger 1995), using $\Omega_b h^2 = 0.211$ for the baryon fraction and $\sigma_8 = 0.73$ for the normalization of the matter power spectrum.

The simulation contained $N = 512^3$ particles in a comoving periodic box $4h^{-1}\text{Mpc}$ on a side, making the particle mass $m_p = 3.57 \times 10^4 h^{-1}M_\odot$. The starting redshift was $z = 53$, and the system was evolved down to $z = 6$. The evolution was carried out with the parallel Tree–Particle–Mesh code TPM (Xu 1995; Bode, Ostriker, & Xu 2000; Bode & Ostriker 2003), using a 1024^3 mesh. The evolution took 1150 PM steps, with particles in dense regions taking up to 19,500 steps. The run was carried out using up to 256 processors on the Terascale Computing System at Pittsburgh Supercomputing Center.

The spline softening length in the tree portion of the code was set to $\epsilon = 0.14 h^{-1}\text{kpc}$. With this softening length, relaxation by $z = 6$ inside the core of a collapsed halo (assuming an NFW density distribution with $c = 12$) will not be significant over the course of the simulation for those objects containing more than 100 particles. The opening angle in the Barnes-Hut criterion used by TPM was $\theta = 0.577$, and the time step parameter $\eta = 0.3$; also, the initial values for locating trees were $A = 2.0$ and $B = 12.5$ — see Bode & Ostriker (2003) for details. In the TPM code, not all regions are treated at full resolution. The limiting density (above which all cells are put into trees for increased resolution) rises with time. By the end of this run, all cells containing more than 18 particles are still being followed at full resolution. Thus this factor is not important if the analysis is limited to halos with over 100 particles.

Dark matter halos are identified using DENMAX scheme (Bertschinger & Gelb 1991), smoothing the density field with a Gaussian length of $300h^{-1}\text{kpc}$. In computing all quantities we include all particles located inside the virial radius of a halo.

3. Results

3.1. Pictures

First, we present visually a distribution of the dark matter mass and dark matter halos of varying masses. Figure 1 shows the distribution of dark matter particles projected onto the x-y plane. Figures (2a,b,c,d,e) show the distributions of dark matter halos with masses greater than ($10^6, 10^{6.5}, 10^7, 10^{7.5}, 10^8$) M_\odot , respectively, at $z = 6$. The progressively stronger clustering of more massive halos is clearly visible in the display but we will return to the clustering properties more quantitatively in §3.3. It is also noted that voids are progressively more visible in the higher mass halos than in low mass halos.

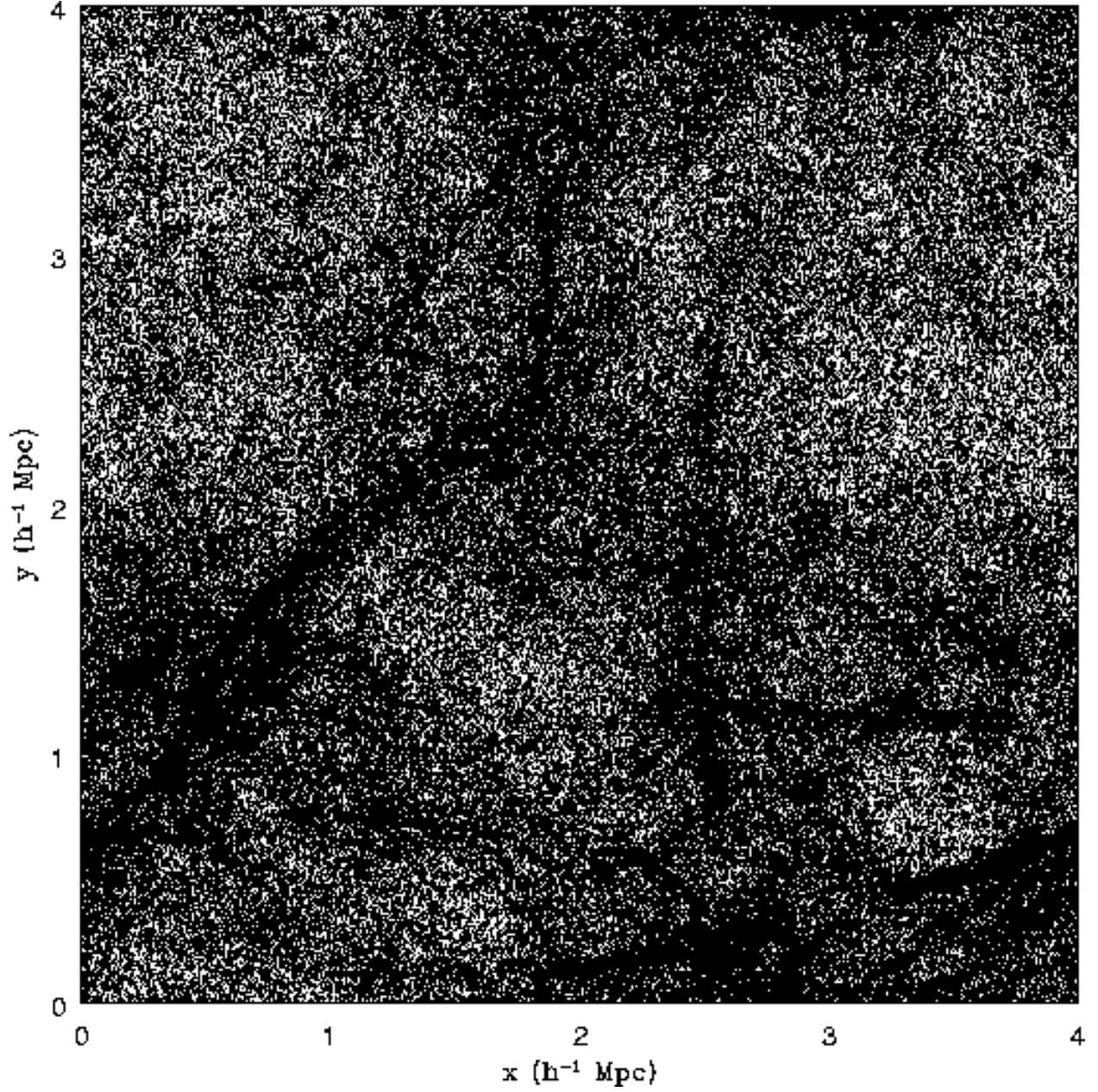


Fig. 1.— The distribution of dark matter particles at $z = 6$ projected onto the x-y plane (0.25% of the total).

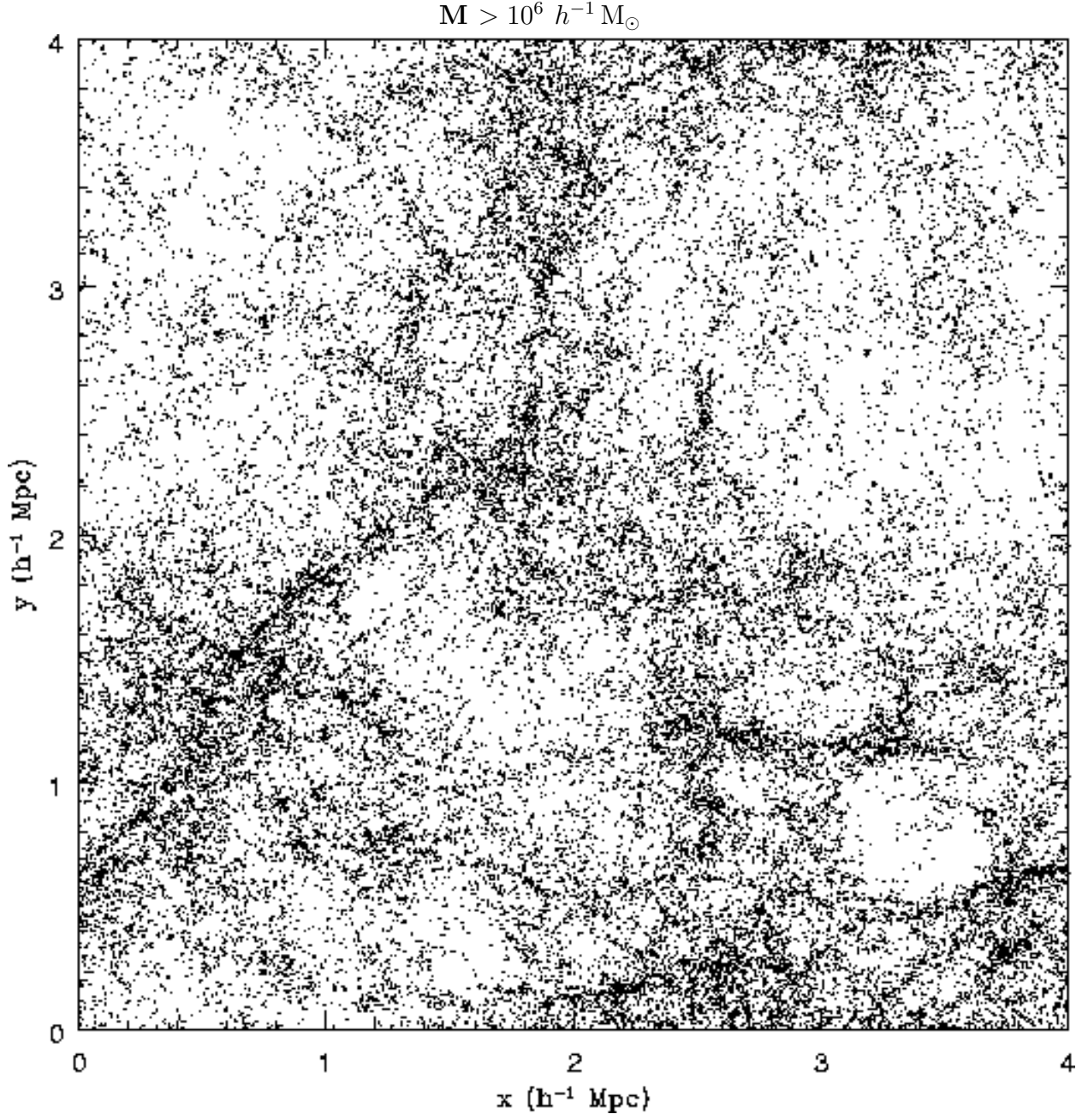


Fig. 2.— The distributions of all dark matter halos with masses greater than $(10^6, 10^{6.5}, 10^7, 10^{7.5}, 10^8) M_{\odot}$, respectively, at $z = 6$.

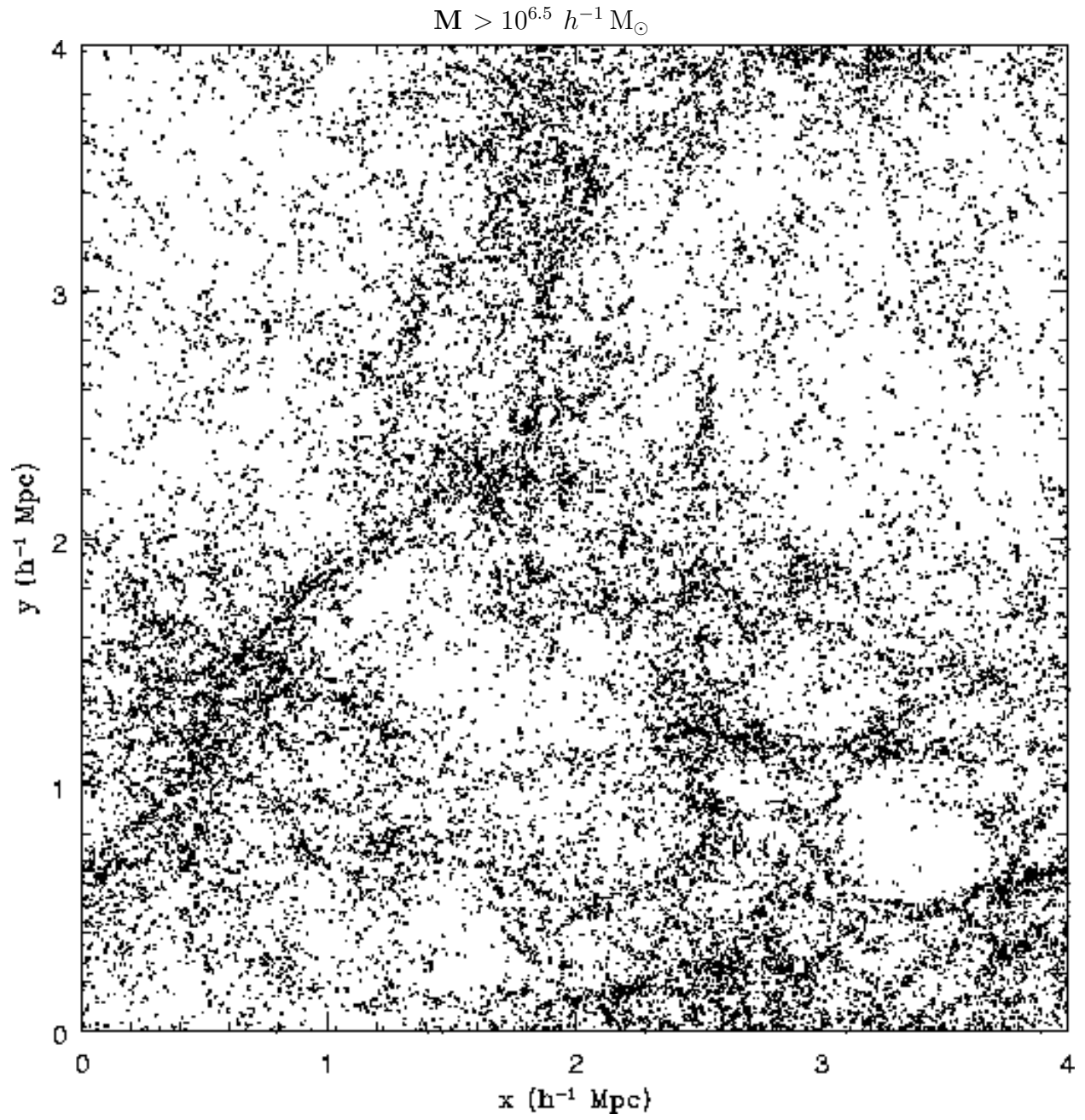


Fig. 2.— Continued.

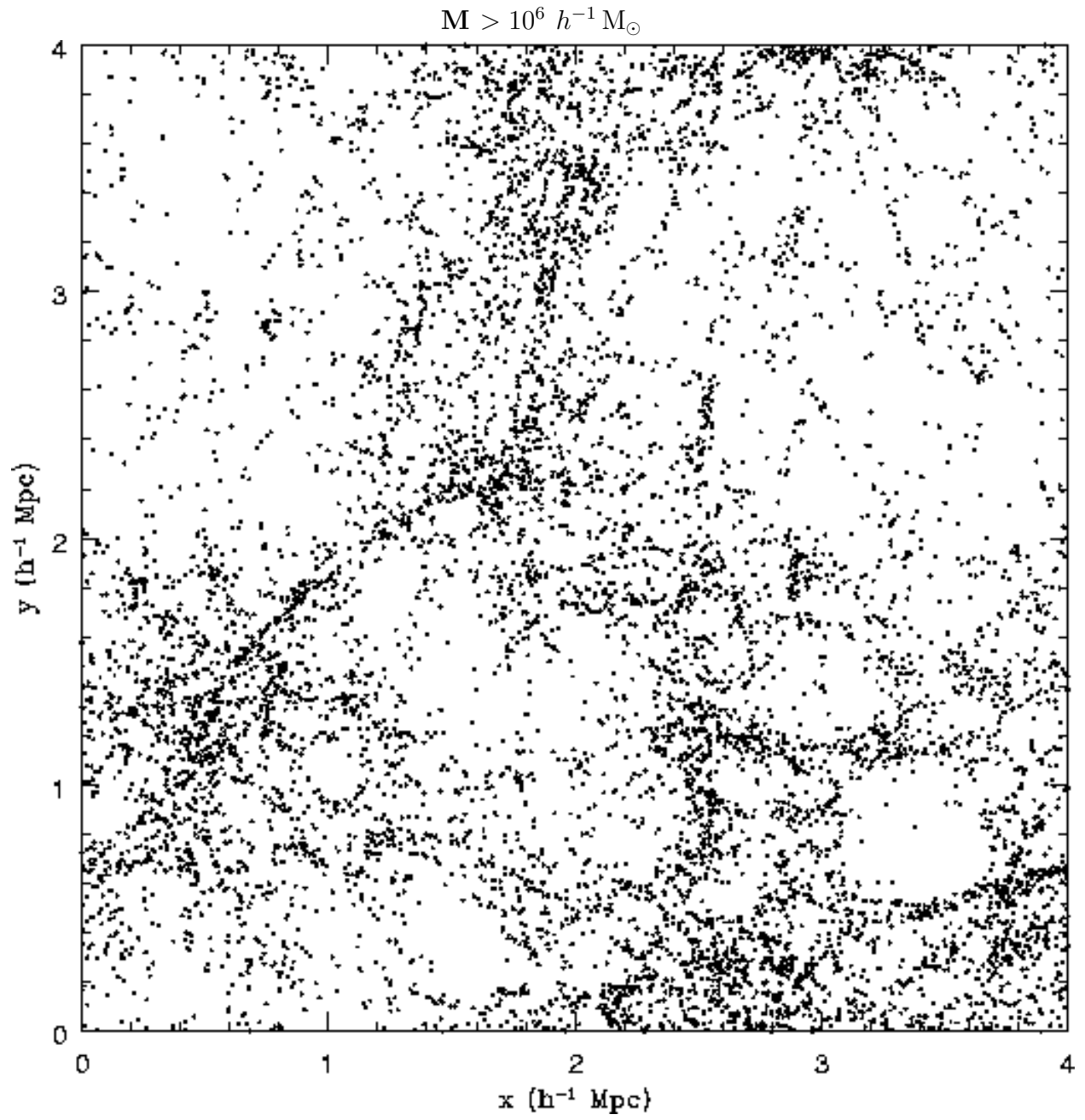


Fig. 2.— Continued.

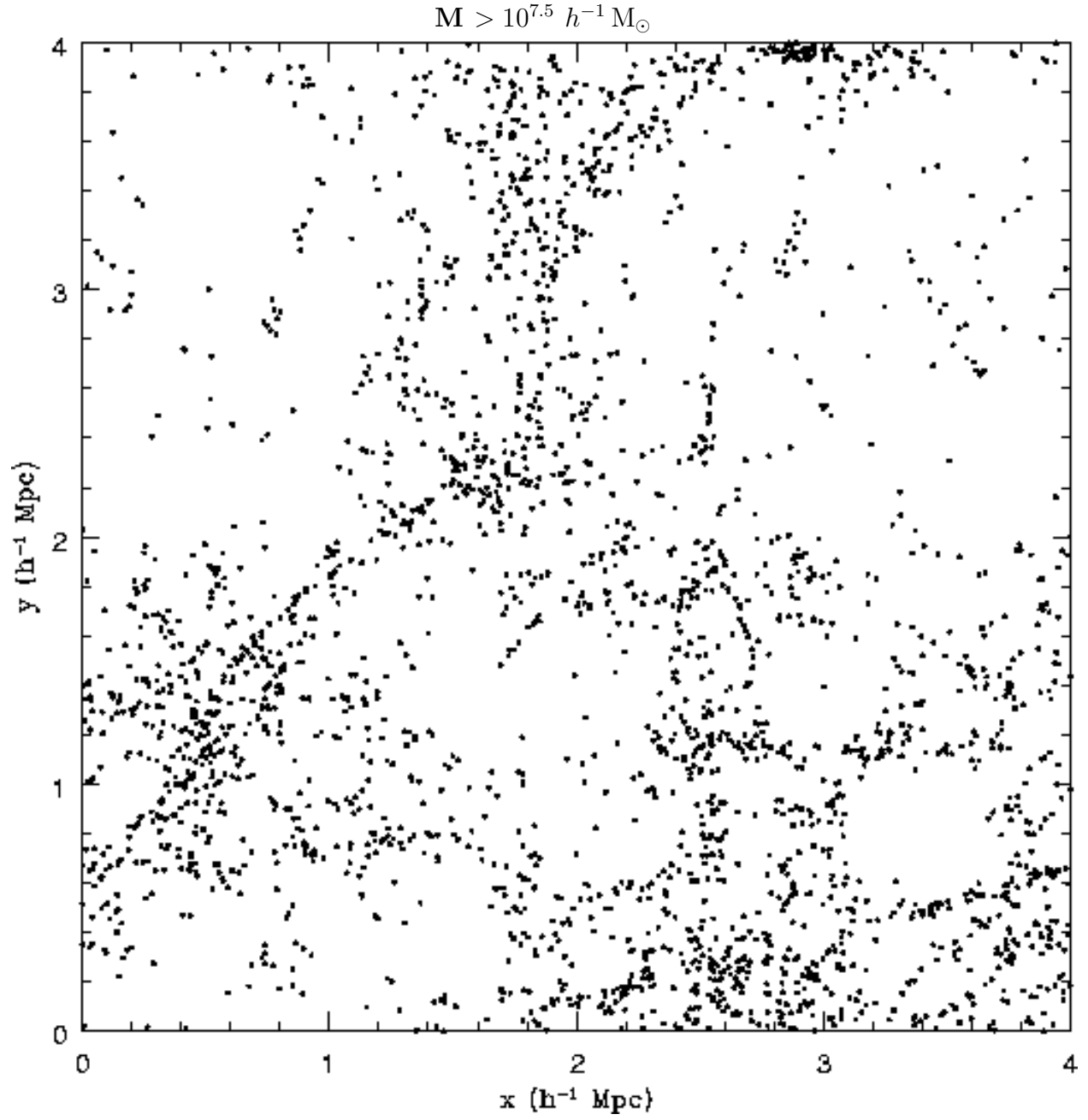


Fig. 2.— Continued.

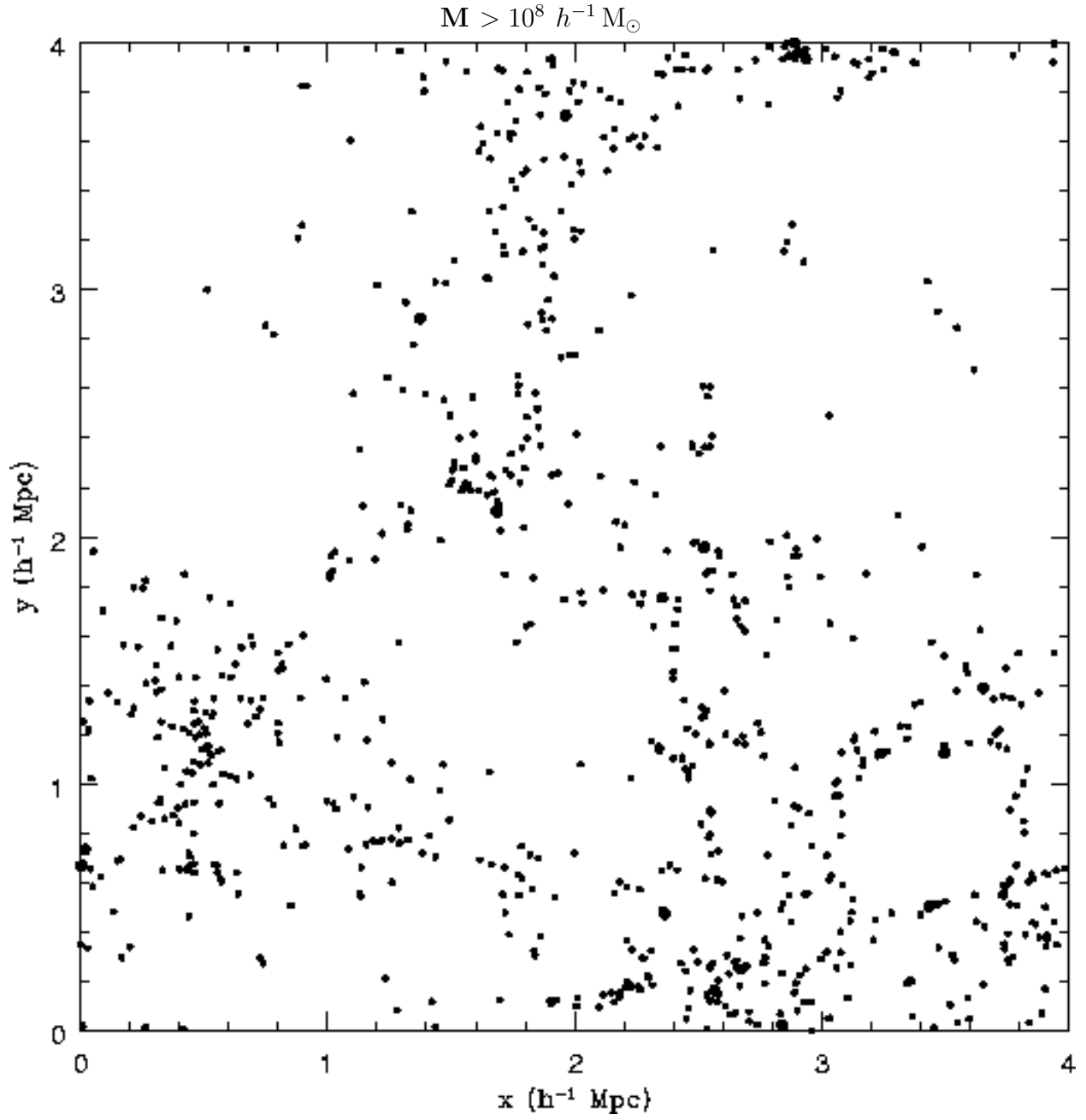


Fig. 2.— Continued.

3.2. Dark Matter Halo Mass Function

Figure 3 shows the halo mass functions at four redshifts. Table 1 summarizes the fitting parameters for a Schechter function of the form

$$n(M)dM = n_0\left(\frac{M}{M_*}\right)^{-\alpha} \exp(-M/M_*)\frac{dM}{M_*}. \quad (1)$$

We see that the Schechter function provides a good fit to the computed halo mass function. The faint end slope is $\alpha = 2.05 \pm 0.15$, consistent with the expectation from Press-Schechter theory (Press & Schechter 1974). While there appears to be a slight steepening of the slope at the low mass end from -1.9 to -2.2 from $z = 6$ to $z = 11.1$, it is unclear, however, how significant this trend is, given the adopted, somewhat degenerate fitting formula. The turnover at $M_h \sim 10^{6.5} M_\odot$ indicates the loss of validity of our simulation at the low mass end.

3.3. Bias of Dark Matter Halos

We characterize the relative distribution of halos over the total dark matter distribution by the following relation:

$$\frac{n_h}{\langle n_h \rangle} = b(M, z)\left(\frac{\rho_m}{\langle \rho_m \rangle}\right)^{c(M, z)}, \quad (2)$$

where n_h and $\langle n_h \rangle$ are the halo density and mean halo density; ρ_m and $\langle \rho_m \rangle$ are the mass density and mean mass density; $c(M, z)$ is fixed to be unity at $\frac{\rho_m}{\langle \rho_m \rangle} > 1$. This empirical fitting formula is motivated by the found result that there appears to be a break in $\frac{n_h}{\langle n_h \rangle}$ at $\frac{\rho_m}{\langle \rho_m \rangle} \sim 1$. Tables 2 and 3 list the parameters $b(M, z)$ and $c(M, z)$. The smoothing length used here is $0.3 h^{-1}$ Mpc. Figure 4 shows four typical cases to indicate the goodness of the fitting formula. At $\frac{\rho_m}{\langle \rho_m \rangle} < 1$ our results (Table 2) indicate $\frac{n_h}{\langle n_h \rangle} \propto \left(\frac{\rho_m}{\langle \rho_m \rangle}\right)^{3-7}$, a

Table 1. Halo Mass Function Fitting Parameters

Parameters	z=6.0	z=7.4	z=9.08	z=11.096
n_0 ($h^3 \text{ Mpc}^{-3}$)	0.85	1.20	1.75	2.40
α	1.9	2.0	2.1	2.2
M_* ($h^{-1} \text{ Mpc}$)	8×10^8	6×10^8	4×10^8	2×10^8

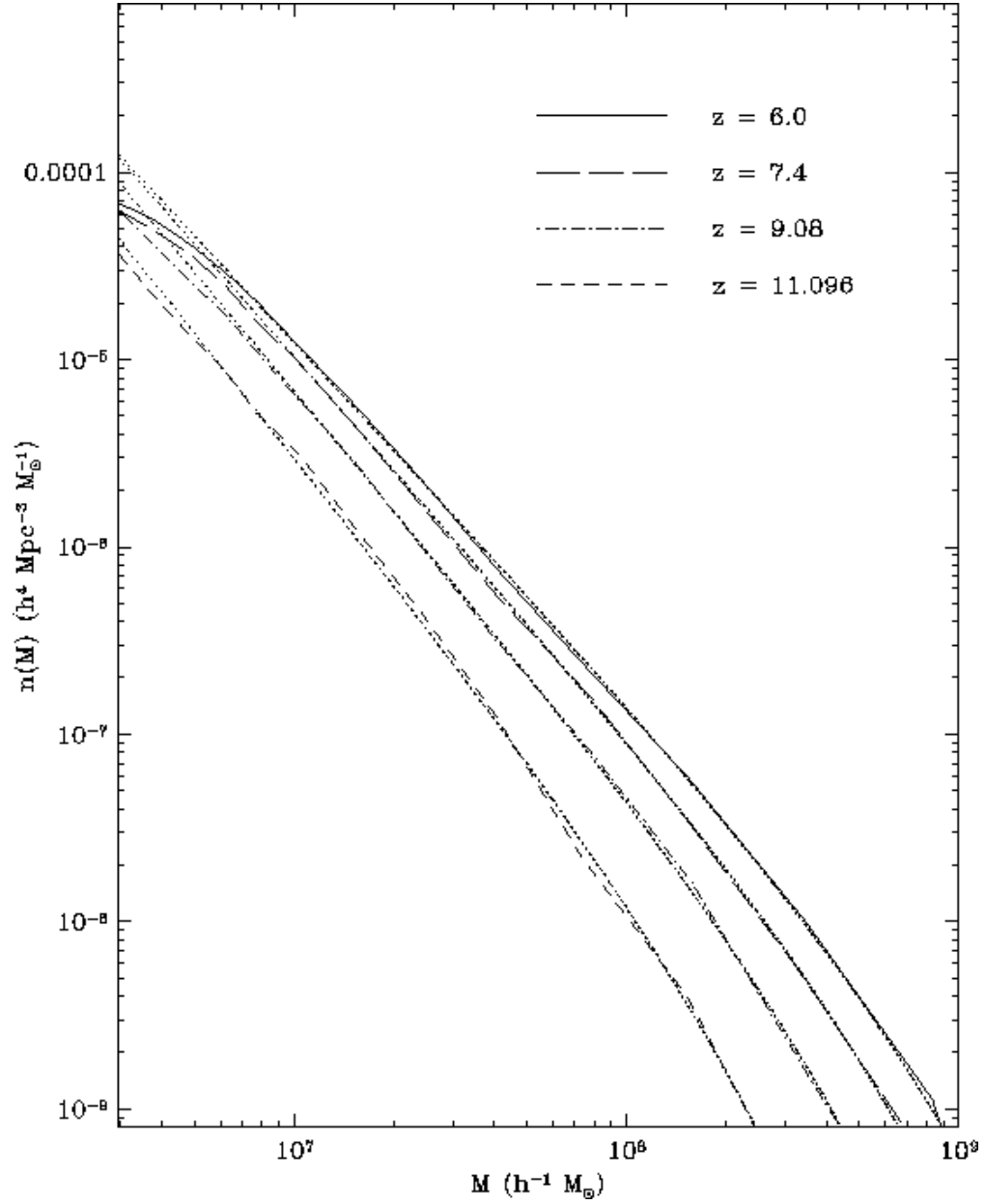


Fig. 3.— The halo mass functions at four redshifts. Dotted lines represent the fitted Schechter functions with parameters summarized in Table 1.

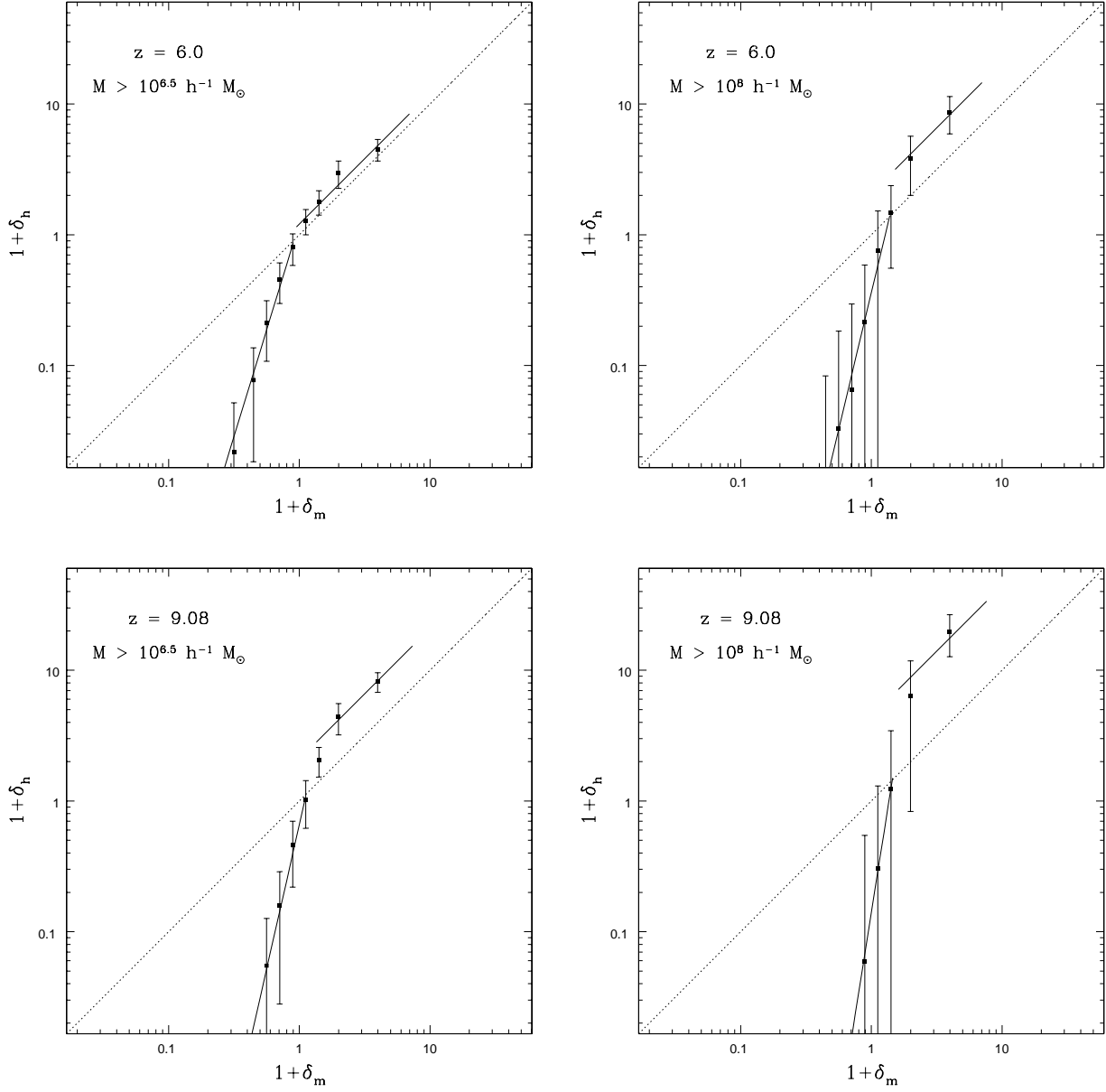


Fig. 4.— Bias of dark matter halos in four randomly selected cases upon different mass and redshift. The darkened lines show the fitting formulae of the bias relation.

Table 2. Halo Bias : $b(M,z)$

Halo Mass ($h^{-1} M_{\odot}$)	$z=6.0$	$z=7.4$	$z=9.08$	$z=11.096$
$>10^{6.0}$	1.16 ± 0.12	1.36 ± 0.18	1.70 ± 0.20	2.46 ± 0.23
$>10^{6.5}$	1.21 ± 0.13	1.45 ± 0.17	2.09 ± 0.30	3.05 ± 0.33
$>10^{7.0}$	1.37 ± 0.19	1.60 ± 0.23	2.77 ± 0.40	3.92 ± 0.90
$>10^{7.5}$	1.72 ± 0.32	2.12 ± 0.47	3.46 ± 0.87	6.17 ± 3.17
$>10^{8.0}$	2.08 ± 0.55	2.58 ± 0.90	4.43 ± 1.47	9.90 ± 4.58

Table 3. Halo Bias : $c(M,z)$

Halo Mass ($h^{-1} M_{\odot}$)	$z=6.0$	$z=7.4$	$z=9.08$	$z=11.096$
$>10^{6.0}$	3.00 ± 0.55	3.80 ± 0.79	4.14 ± 0.80	4.90 ± 1.49
$>10^{6.5}$	3.27 ± 0.71	4.20 ± 1.04	4.41 ± 1.31	5.52 ± 2.43
$>10^{7.0}$	3.43 ± 0.70	4.37 ± 1.07	4.97 ± 2.59	7.33 ± 6.29
$>10^{7.5}$	3.93 ± 1.70	4.98 ± 2.96	5.09 ± 3.31	7.41 ± 9.09
$>10^{8.0}$	4.18 ± 2.28	5.61 ± 4.68	6.32 ± 6.12	6.77 ± 8.90

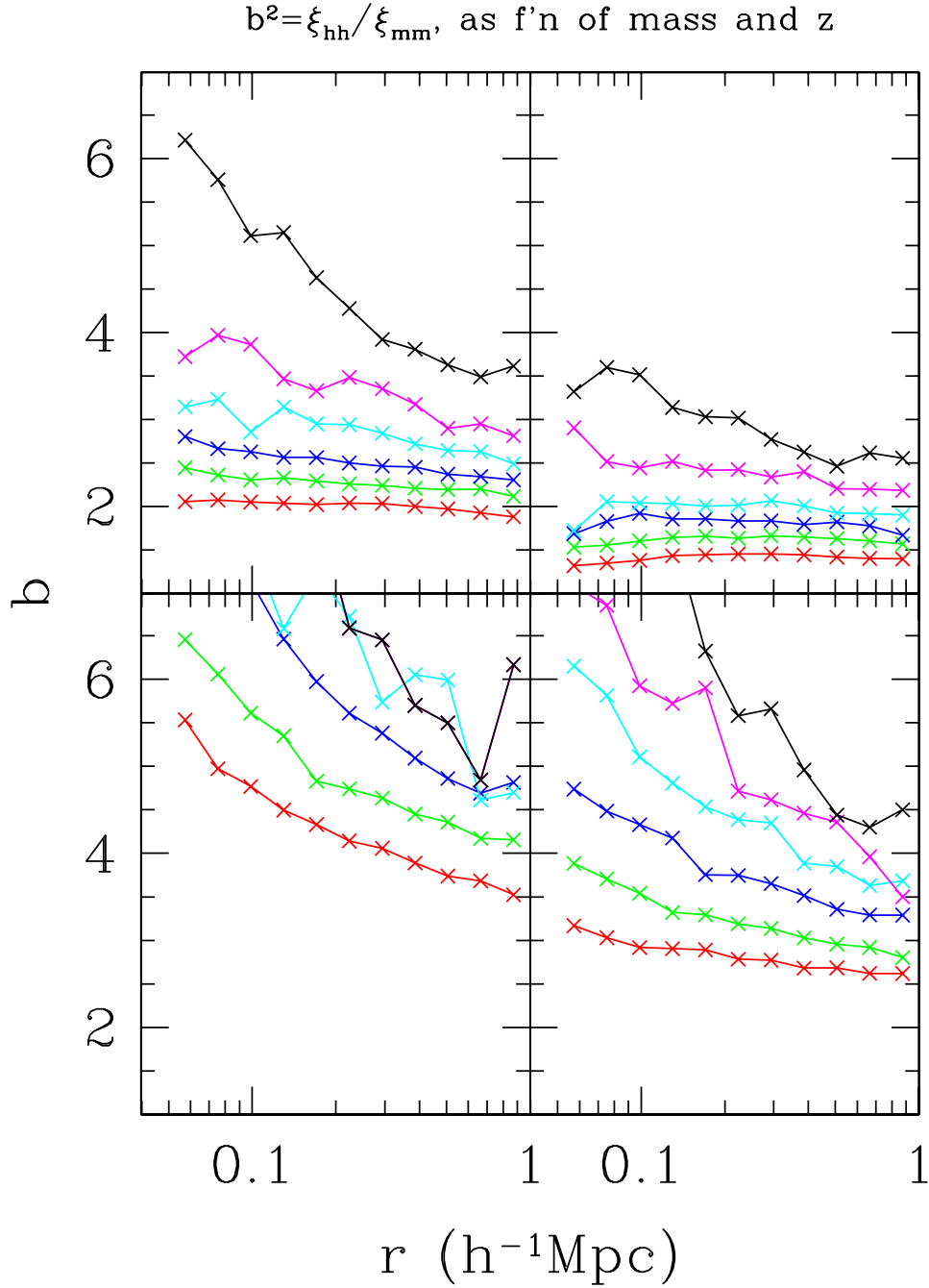


Fig. 5.— shows the ratio of dark matter halo correlation function over the dark matter mass correlation function at four redshifts, $z = 6.0$ (top right panel), $z = 7.4$ (top left), $z = 9.1$ (bottom right) and $z = 11$ (bottom left). In each panel six curves are shown for halos more massive than $10^6 M_\odot$, $10^{6.5} M_\odot$, $10^7 M_\odot$, $10^{7.5} M_\odot$, $10^8 M_\odot$ and $10^{8.5} M_\odot$, respectively.

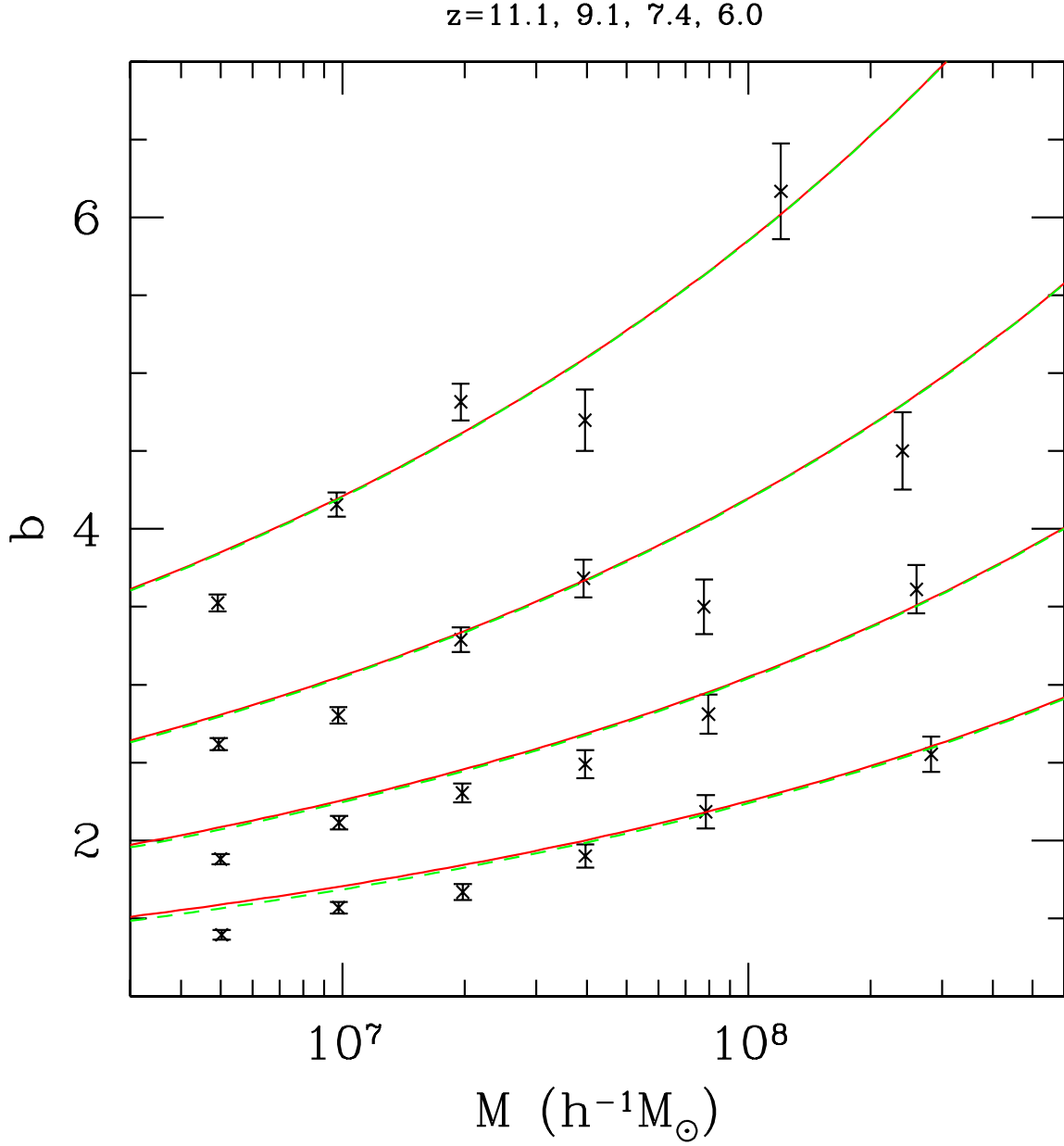


Fig. 6.— shows the bias as a function of halo mass at redshifts $z = (6, 7.4, 9.1, 11.1)$ at separation of $1h^{-1}\text{Mpc}$ as symbols (x). The curves are computed using the analytic method of Mo & White (1996).

rather rapid drop. As expected, the drop-off is more dramatic for larger halos, as visible in Figure 2. This implies that at $z > 6$ halos are unlikely to be found in underdense regions (on a scale of $\sim 0.3Mpc/h$). The increase of $c(M, z)$ with redshift implies that voids are emptier at higher redshifts.

Another way to characterize the relative distribution of dark matter halos over mass is to compute the ratio of the correlation functions, which are shown in Figure 5. The correlation function $\xi(r)$ is calculated by counting the number of pairs of either particles or halos at separation r (using logarithmically spaced bins) and comparing that number to a Poisson distribution. It can be seen that the bias falls in the range 2 – 6, with the trend that the more massive halos are more biased and at a fixed mass halos at higher redshifts are more biased, as expected. Figure 6 recollects the information in Figure 5 and shows the bias as a function of halo mass at four different redshifts at the scale chosen to be $1h^{-1}Mpc$. The agreement between our computed results and that using analytic method of Mo & White (1996) is good, indicating that the latter is valid for objects at scales and redshifts of concern here.

3.4. Dark Matter Halo Density Profile

We use a variant fitting formula based on the NFW (Navarro, Frenk, & White 1997) profile:

$$\rho_r = \frac{\rho_s}{\left(\frac{r}{r_{-2}}\right)^\alpha \left(1 + \frac{r}{r_{-2}}\right)^{4-2\alpha}}. \quad (3)$$

Note that for NFW profile, $\alpha = 1$. An important difference, however, is the scaling radius used. We use the radius where the logarithmic slope of the density profile is -2 , r_{-2} , instead of the more conventional “core” radius. This is a two parameter fitting formula, α and r_{-2} , while ρ_s is a function of α and r_{-2} at a fixed redshift, since the overdensity interior to the virial radius r_v is assumed to be known. This fitting formula is intended for the range in radius $r \leq r_v$ only.

We fit the density profile of each halo using the least squares method. Four randomly selected examples of such profiles along with the fitted curve using Equation (3) are shown in Figure 7, indicating reasonable fits in all cases. Both fitting parameters, α and r_{-2} , however, display broad distributions. We found that there is only weak correlation between α and r_{-2} . Figure 8 shows histograms for the distributions of α , for four typical cases. We fit α

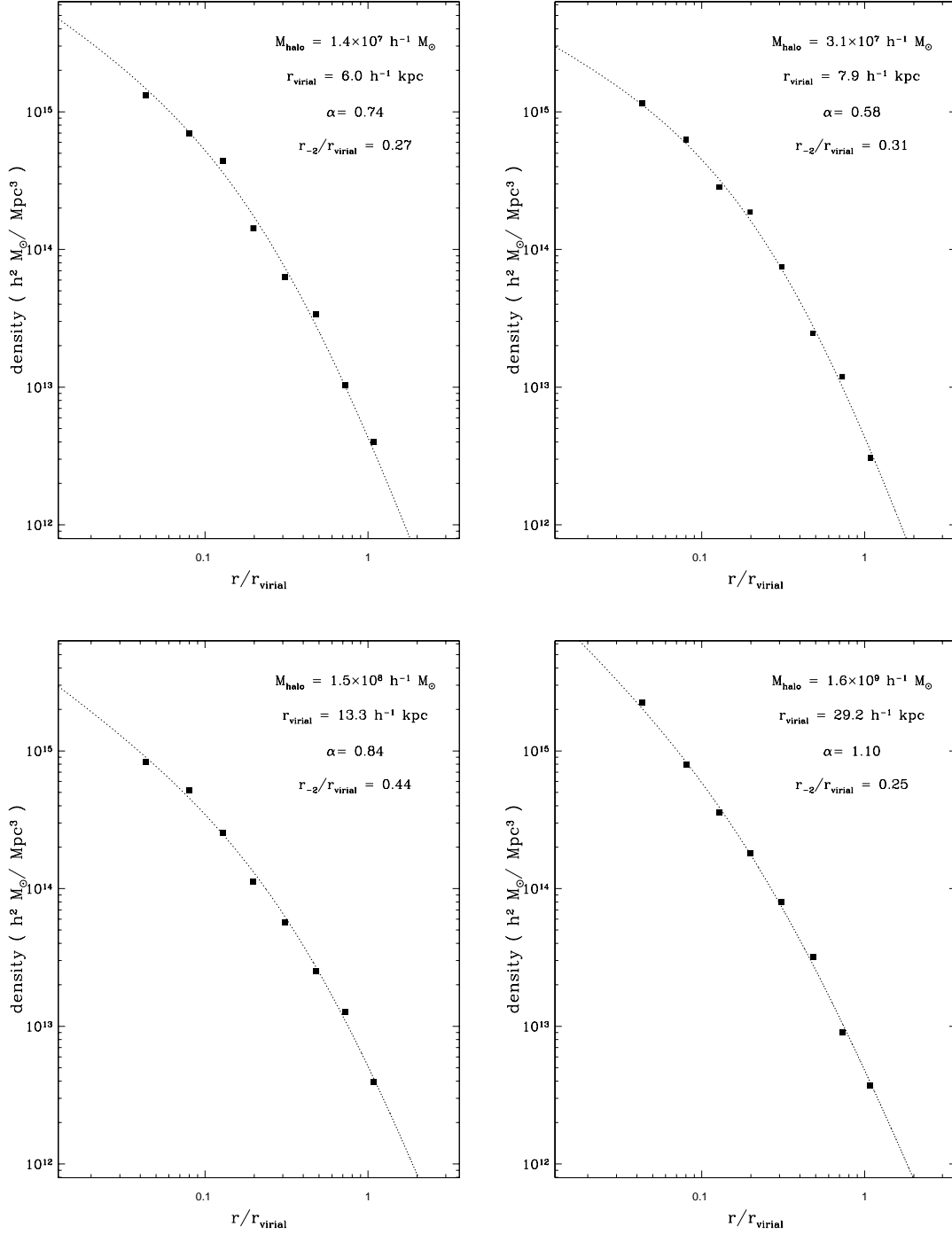


Fig. 7.— Density profiles of four randomly selected halos over a mass range at $z = 6$. The dotted lines represent the best-fit modified NFW relation given in Section 3.

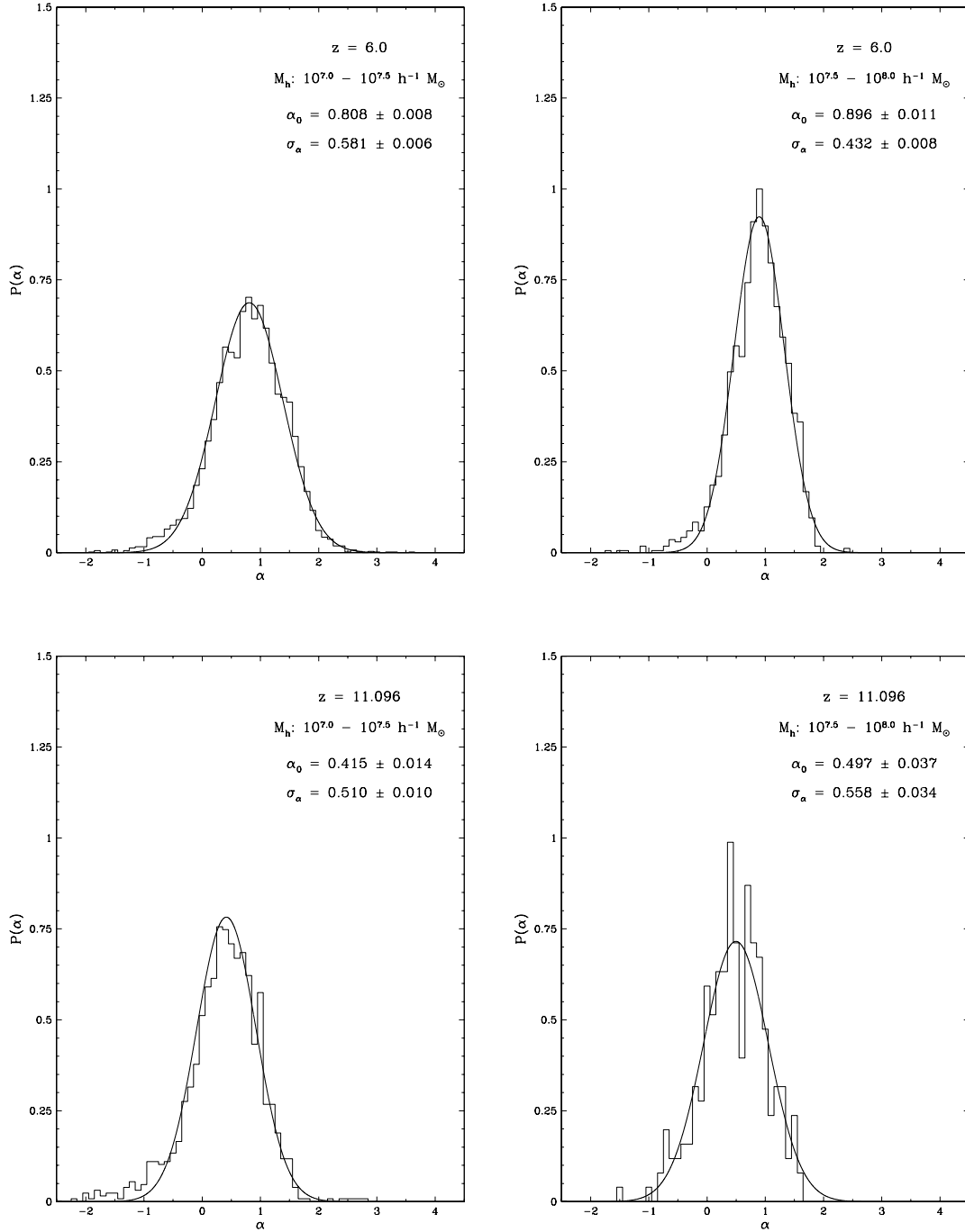


Fig. 8.— The distributions of inner slope parameter α in the halo density profile fitting for four randomly selected cases upon different mass and redshift. The Gaussian fits are shown as smooth curves.

distributions using a Gaussian distribution function:

$$P(\alpha) = \frac{1}{\sqrt{2\pi}\sigma_\alpha} \exp\left(-\frac{(\alpha - \alpha_0)^2}{2\sigma_\alpha^2}\right). \quad (4)$$

The Gaussian fits are shown as smooth curves in Figure 8, demonstrating that the proposed Gaussian fits are good. Tables 4,5 list fitting parameters α_0 and σ_{α_0} , respectively. We recollect the data in Table 4 and shows in Figure 9 the median inner density slope as a function of dark matter halo different mass at four different redshifts (symbols). The curves in Figure 9 are empirical fits using the following formula

$$\alpha_0 = 0.75((1+z)/7.0)^{-1.25}(M/10^7 M_\odot)^{0.11(1+z)/7.0}. \quad (5)$$

It is seen that this fitting formula provides a reasonable fit for the simulated halos.

Figure 10 shows histograms for the distributions of r_{-2} for four typical cases. We fit r_{-2} distributions using a lognormal function:

$$P(r_{-2}) = \frac{1}{r_{-2}\sqrt{2\pi}\sigma_{r_{-2}}} \exp\left(-\frac{(\ln r_{-2} - \ln r_{-2}^0)^2}{2\sigma_{r_{-2}}^2}\right), \quad (6)$$

which are seen to provide reasonable fits to the data in Figure 10. Tables 6,7 list fitting parameters r_{-2}^0 and $\sigma_{r_{-2}}$, respectively. We find no visible correlation between α and r_{-2} , as shown in Figure 11.

An important point to note is that the average slope of the density profiles of small halos ranges from 1.0 to 0.4 from $z = 6$ to $z = 11$ (Table 4 and Figure 8), which is somewhat shallower than the universal density profile found by Navarro et al. (1997). Our results at $z = 9 - 11$ are in good agreement with Ricotti (2003), who simulated a $1h^{-1}\text{Mpc}$ box for small halos at $z = 10$. If the theoretical argument for the dependence of halo density profile on the slope of the initial density fluctuation power spectrum (Syer & White 1988; Subramanian, Cen, & Ostriker 2000) is correct, as adopted by Ricotti (2003) to explain the

Table 4. Density Profile : $\alpha_0(M, z)$

Halo Mass ($h^{-1} M_\odot$)	z=6.0	z=7.4	z=9.08	z=11.096
$10^{7.0} - 10^{7.5}$	0.81 ± 0.01	0.63 ± 0.01	0.50 ± 0.01	0.42 ± 0.01
$10^{7.5} - 10^{8.0}$	0.90 ± 0.01	0.75 ± 0.02	0.62 ± 0.02	0.50 ± 0.04
$> 10^{8.0}$	1.09 ± 0.02	0.91 ± 0.02	0.77 ± 0.03	0.65 ± 0.06

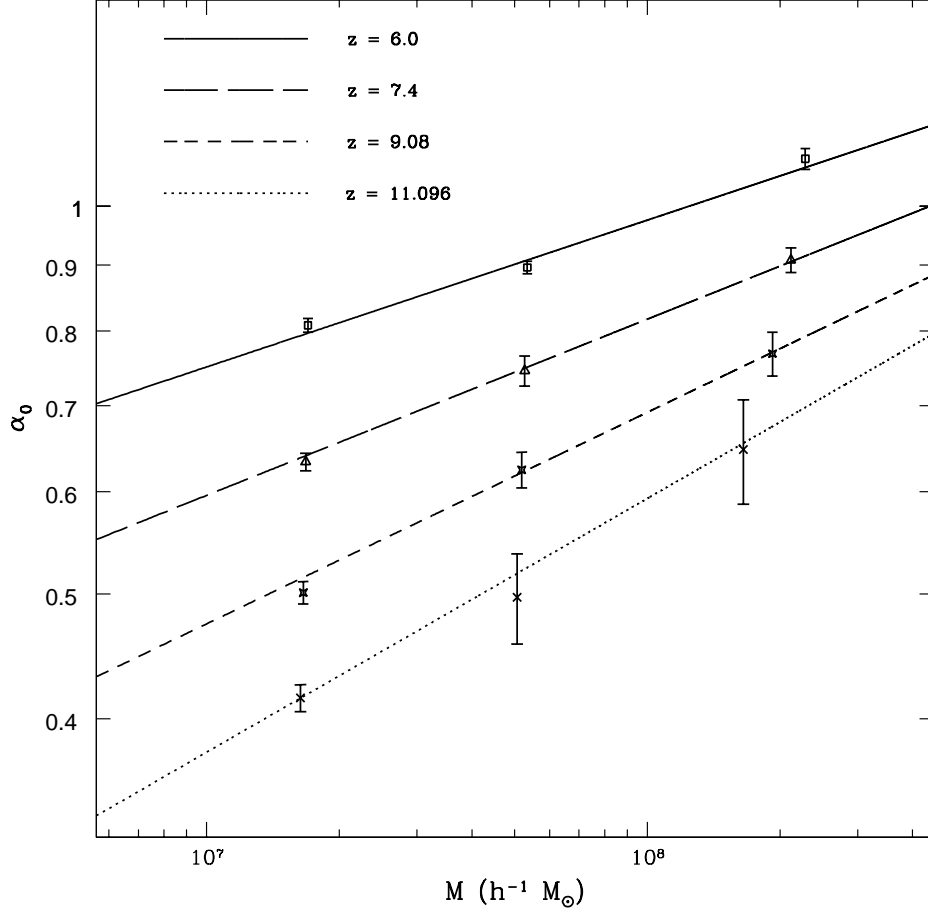


Fig. 9.— shows the median inner density slope as a function of dark matter halo different mass at four different redshifts (symbols). The curves are fits (Equation 5).

Table 5. Density Profile : $\sigma_\alpha(M, z)$

Halo Mass ($h^{-1} M_\odot$)	$z=6.0$	$z=7.4$	$z=9.08$	$z=11.096$
$10^{7.0} - 10^{7.5}$	0.58 ± 0.01	0.54 ± 0.01	0.52 ± 0.01	0.51 ± 0.01
$10^{7.5} - 10^{8.0}$	0.43 ± 0.01	0.45 ± 0.01	0.46 ± 0.02	0.56 ± 0.03
$> 10^{8.0}$	0.41 ± 0.01	0.41 ± 0.02	0.41 ± 0.03	0.38 ± 0.06

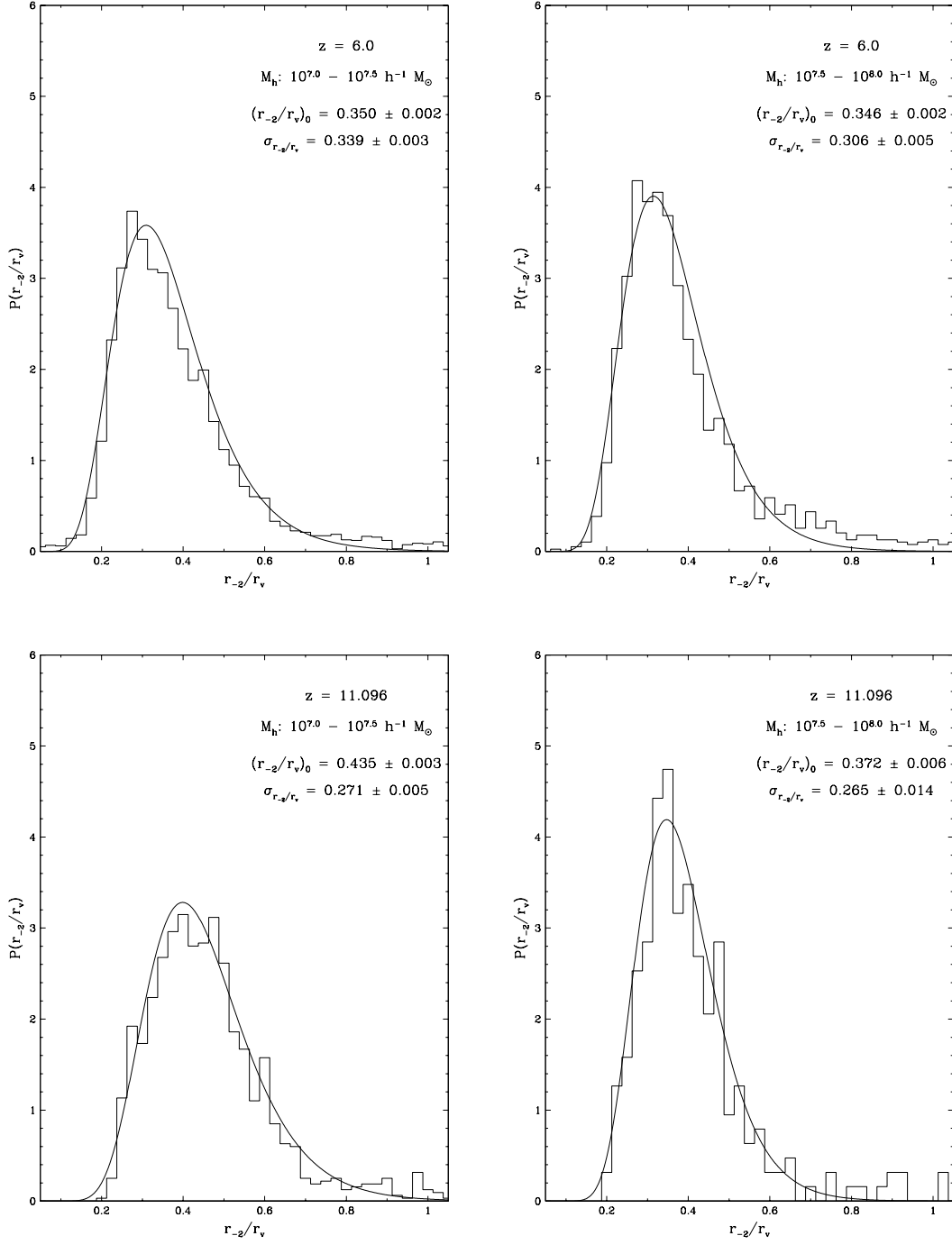


Fig. 10.— The distributions of radius parameter r_{-2} in the halo density profile fitting for four randomly selected cases upon different mass and redshift. The lognormal fits are shown as smooth curves.

dependence of inner density slope on halo mass, it then follows that the neglect of density fluctuations on scales larger than his box size of $1h^{-1}\text{Mpc}$ in Ricotti (2003) would make the density profiles of the halos in his simulation somewhat shallower than they should be in the CDM model. Thus, the difference in the box size ($1h^{-1}\text{Mpc}$ in Ricotti 2003 versus $4h^{-1}\text{Mpc}$ for our simulation box) would have expected to result in a slightly steeper inner slope in our simulation, which is indeed the case.

Another point to note, which is not new but not widely known, is that there is a large dispersion in the inner slope of order 0.5 due to the intrinsically stochastic nature of halo assembly. This was found earlier by Subramanian et al. (2000). Therefore, while a “universal” profile is informative in characterizing the mode, a dispersion would be needed to give a full account. This is particularly important for applications where the dependence on the inner slope is very strong, e.g., strong gravitational lensing. More relevant for our case of small halos is that, for example, the fraction of small halos with inner slope close to zero (i.e., flat core) is non-negligible at $z = 6$. A proper statistical comparison with observations of local dwarf galaxies, however, is not possible with the current simulation without evolving small galaxies to $z = 0$.

Also worthwhile is to understand whether or not there is some dependence of the inner slope of the density profile on the central density of a halo or the environmental density where a halo sits. In Figures 12 and 13 we show the correlation between the inner slope of the density profile, α , and the central density of the halo, and between α and the environmental density, respectively. We find no visible correlations between either pair of quantities. But a relationship between halo shape and environment might have been missed due to stochastic variations. Thus, we have checked to see if deviation $\Delta\alpha$, between computed and predicted (based on mass and epoch using equation 5) slope exists. Figure 14 shows this and no correlation is seen. We note that the abundances of halos in the mass range of interest here are on the rise in the redshift range considered (Lacey & Cole 1993), as evident in Figure 3. During this period halos considered the inner density profiles of halos steepen with

Table 6. Density Profile : $r_{-2}^0(M,z)$

Halo Mass ($h^{-1} M_{\odot}$)	z=6.0	z=7.4	z=9.08	z=11.096
$10^{7.0} - 10^{7.5}$	0.35 ± 0.01	0.40 ± 0.01	0.43 ± 0.01	0.44 ± 0.01
$10^{7.5} - 10^{8.0}$	0.35 ± 0.01	0.38 ± 0.01	0.39 ± 0.01	0.37 ± 0.01
$> 10^{8.0}$	0.34 ± 0.01	0.35 ± 0.01	0.34 ± 0.01	0.34 ± 0.02

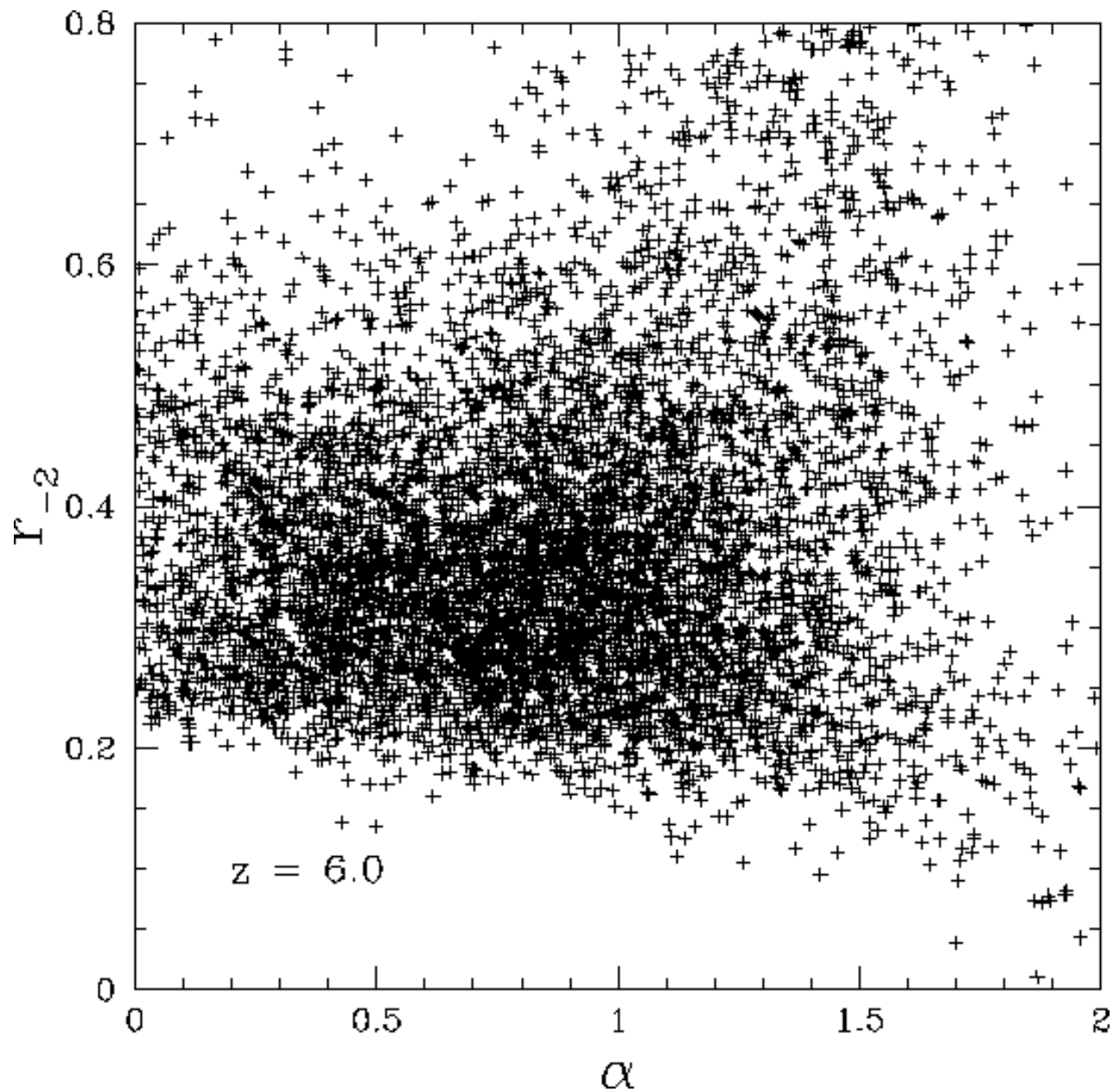


Fig. 11.— A scatter plot of the inner slope of the density profile, α , versus r_{-2} for all the halos with $M > 10^{6.5} h^{-1} M_{\odot}$ at $z = 6$.

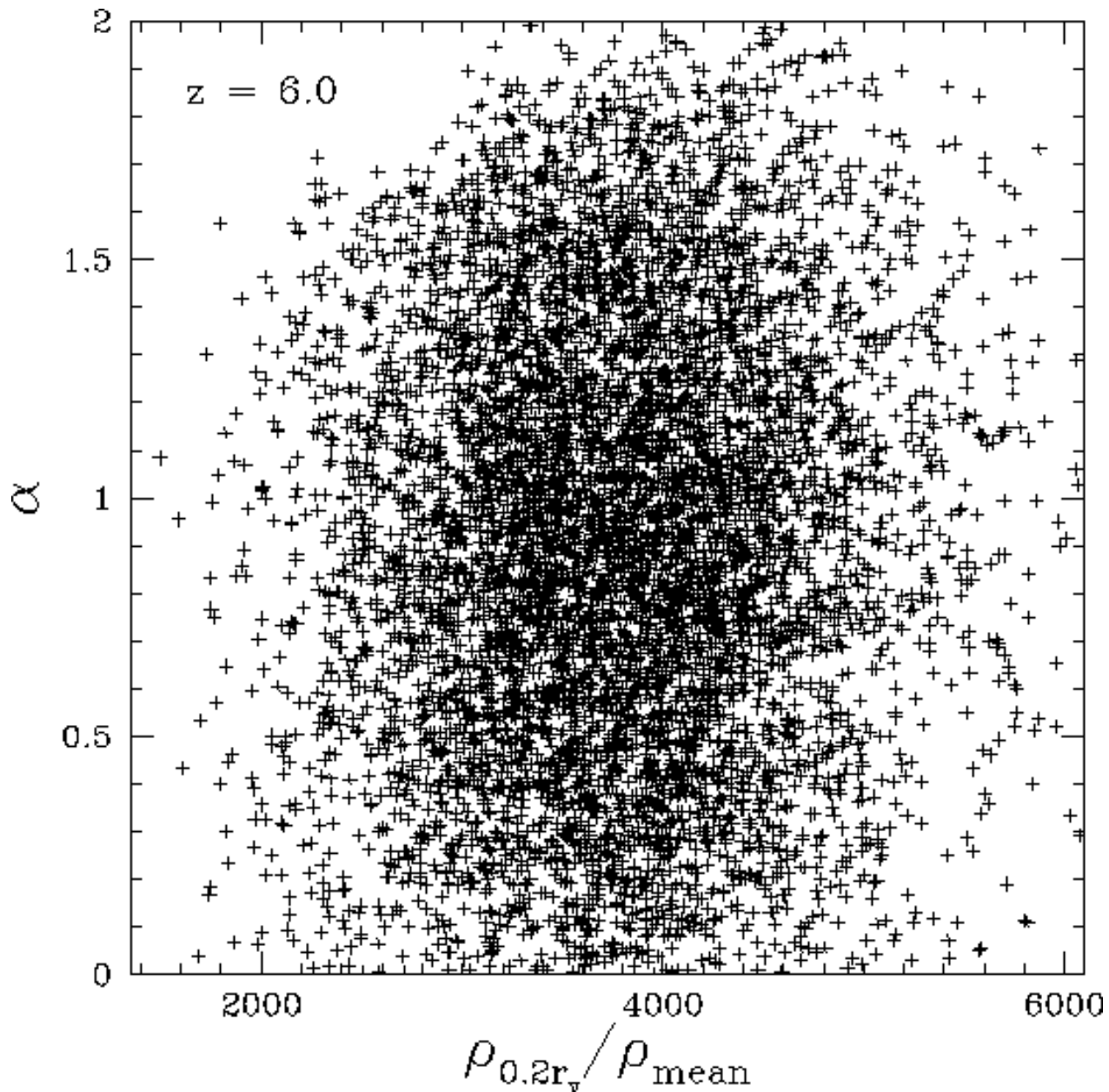


Fig. 12.— A scatter plot of the inner slope of the density profile, α , versus the halo central density, defined as the density at $r < 0.2r_v$, for all the halos with $M > 10^6 h^{-1}M_\odot$ at $z = 6$.

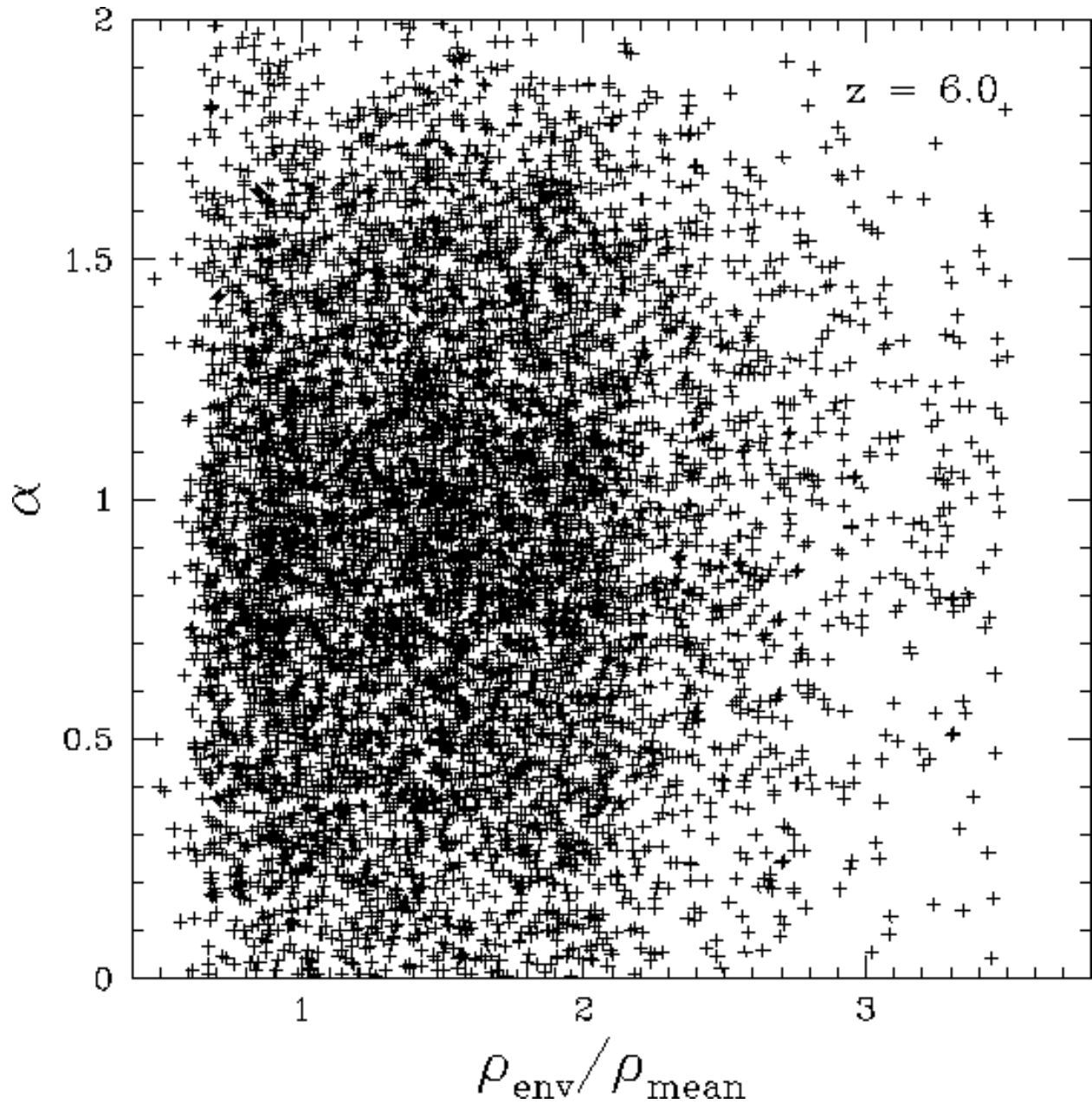


Fig. 13.— A scatter plot of the inner slope of the density profile, α , versus the environmental density, defined as the dark matter density smoothed by a gaussian window of radius $0.3h^{-1}\text{Mpc}$, for all the halos with $M > 10^6 h^{-1}M_{\odot}$ at $z = 6$.

time, consistent with the increase of logarithmic slope of the power spectrum with time, that corresponds to the evolving nonlinear mass scale. However, at some lower redshift not probed here, low mass halos will cease to form. Subsequently, the evolution of halo density profile may show distinct features and some conceivable correlations, not seen in Figures 12 and 13, may show up. We will study this issue separately.

Since the central density of a halo may be considered a good proxy for the formation redshift of the central region, the non-correlation between α and the central density indicates that, for halos of question here, the subsequent process of accretion of mass onto halos is largely a random process, independent of the density of the initial central “seed”. The fact that halos of different masses show a comparable range of central density (not shown in figures) suggest that halos of varying masses form nearly simultaneously, dictated by the nature of the cold dark matter power spectrum at the high- k end; i.e., density fluctuations on those scales involved here depend weakly (logarithmically) on the mass. The non-correlation between the inner slope of the halo density profile and the environmental density may be interpreted in the following way. One may regard regions of different overdensities as local mini-universes of varying density parameters. The independence of the inner slope on local density is thus consistent with published results that the halo density profiles in universes of different Ω_M do not significantly vary.

3.5. Spin Parameter For Dark Matter Halos

We compute the spin parameter defined as

$$\lambda \equiv \frac{J|E|^{1/2}}{GM^{5/2}} \tag{7}$$

(Peebles 1969), where G is the gravitational constant; M is the total mass of the dark matter halo; J is the total angular momentum of the dark matter halo; E is the total energy of

Table 7. Density Profile : $\sigma_{r-2}(M,z)$

Halo Mass ($h^{-1} M_{\odot}$)	$z=6.0$	$z=7.4$	$z=9.08$	$z=11.096$
$10^{7.0} - 10^{7.5}$	0.34 ± 0.01	0.32 ± 0.01	0.29 ± 0.01	0.27 ± 0.01
$10^{7.5} - 10^{8.0}$	0.31 ± 0.01	0.31 ± 0.01	0.27 ± 0.01	0.27 ± 0.01
$> 10^{8.0}$	0.33 ± 0.01	0.25 ± 0.01	0.26 ± 0.02	0.27 ± 0.05

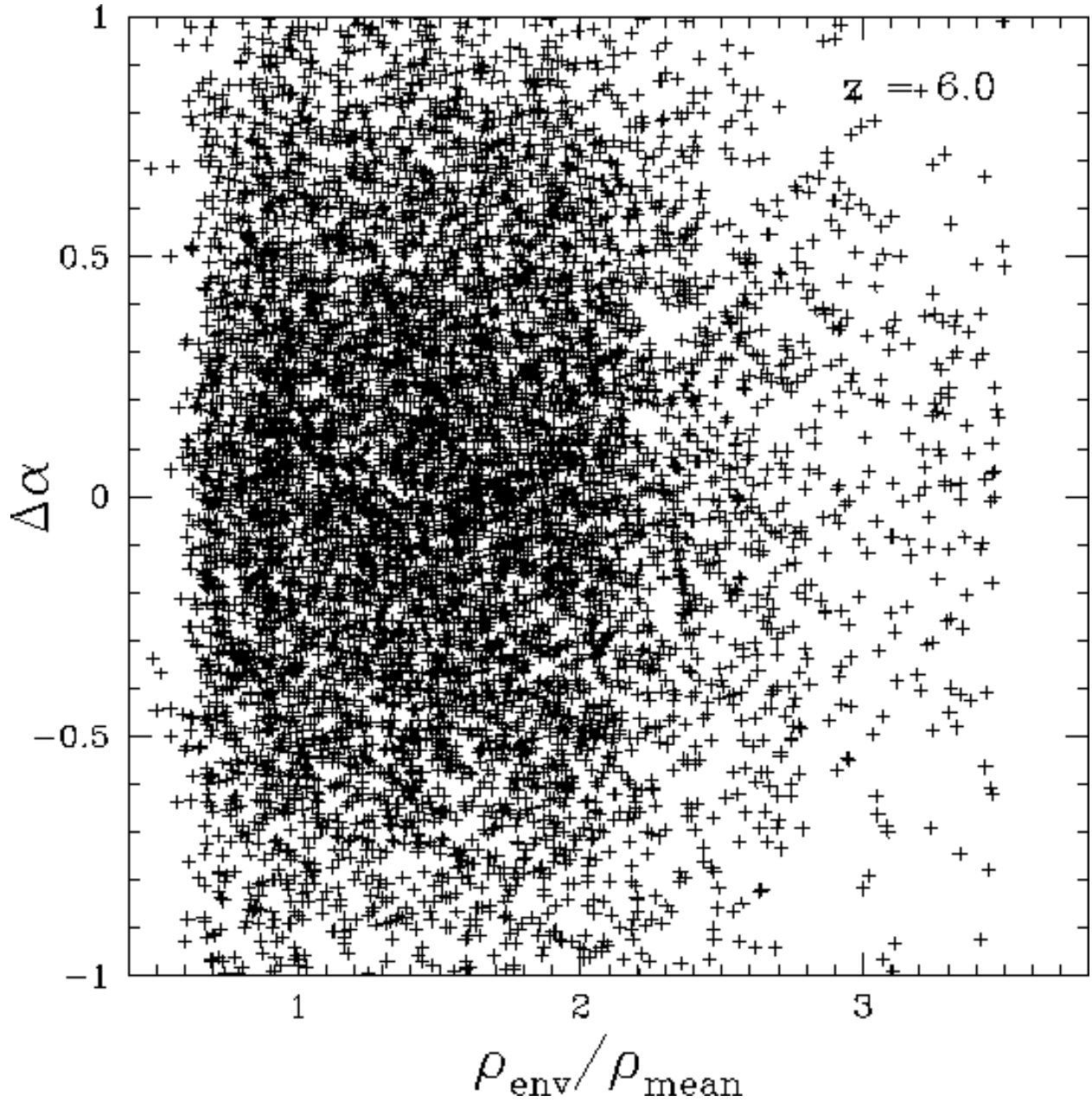


Fig. 14.— A scatter plot of the difference between measured inner slope of the density profile, α , and the fitted inner slope using equation (5), versus the environmental density.

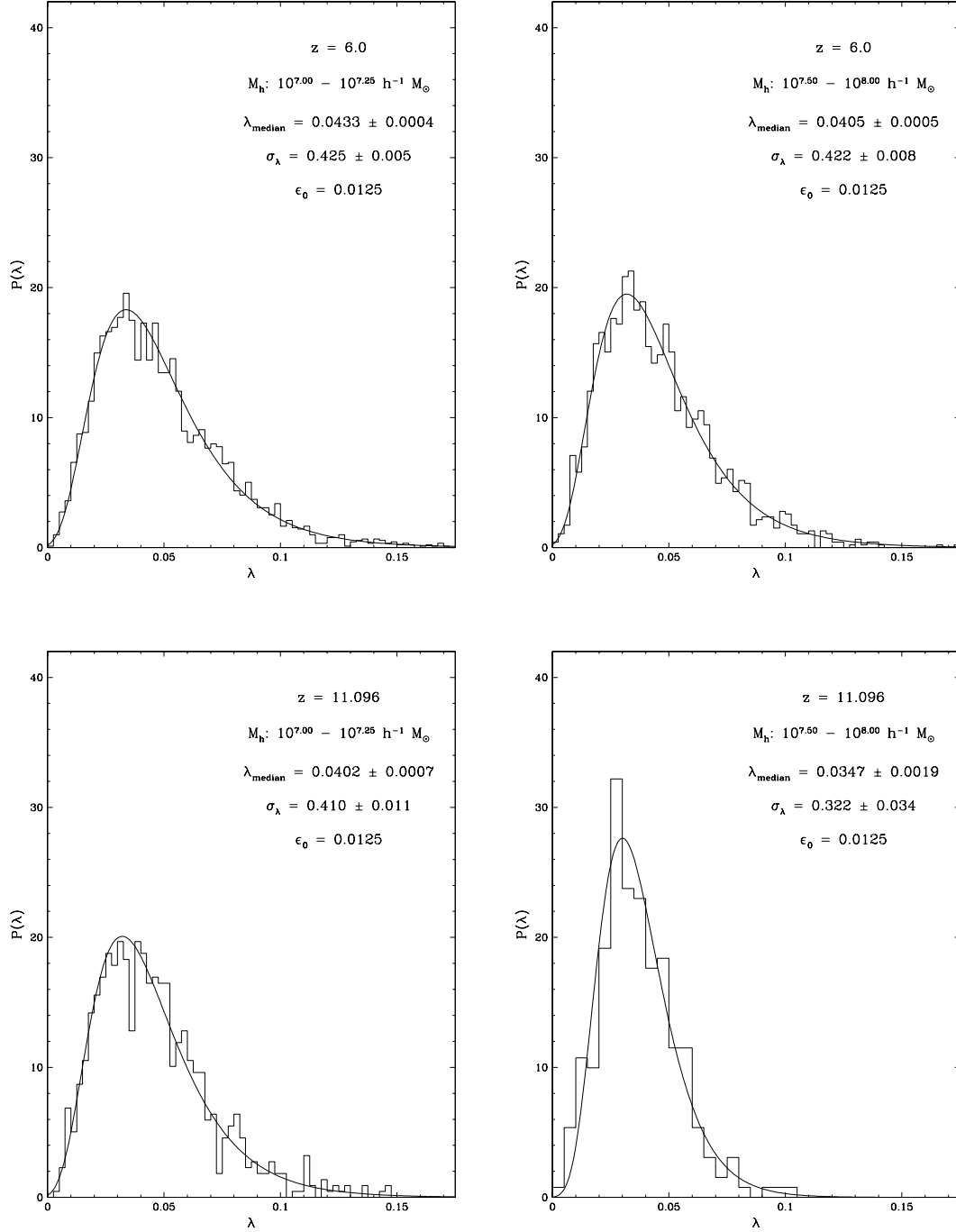


Fig. 15.— The distributions of halo spin parameter λ for four randomly selected cases upon different mass and redshift. The modified lognormal fits are shown as smooth curves.

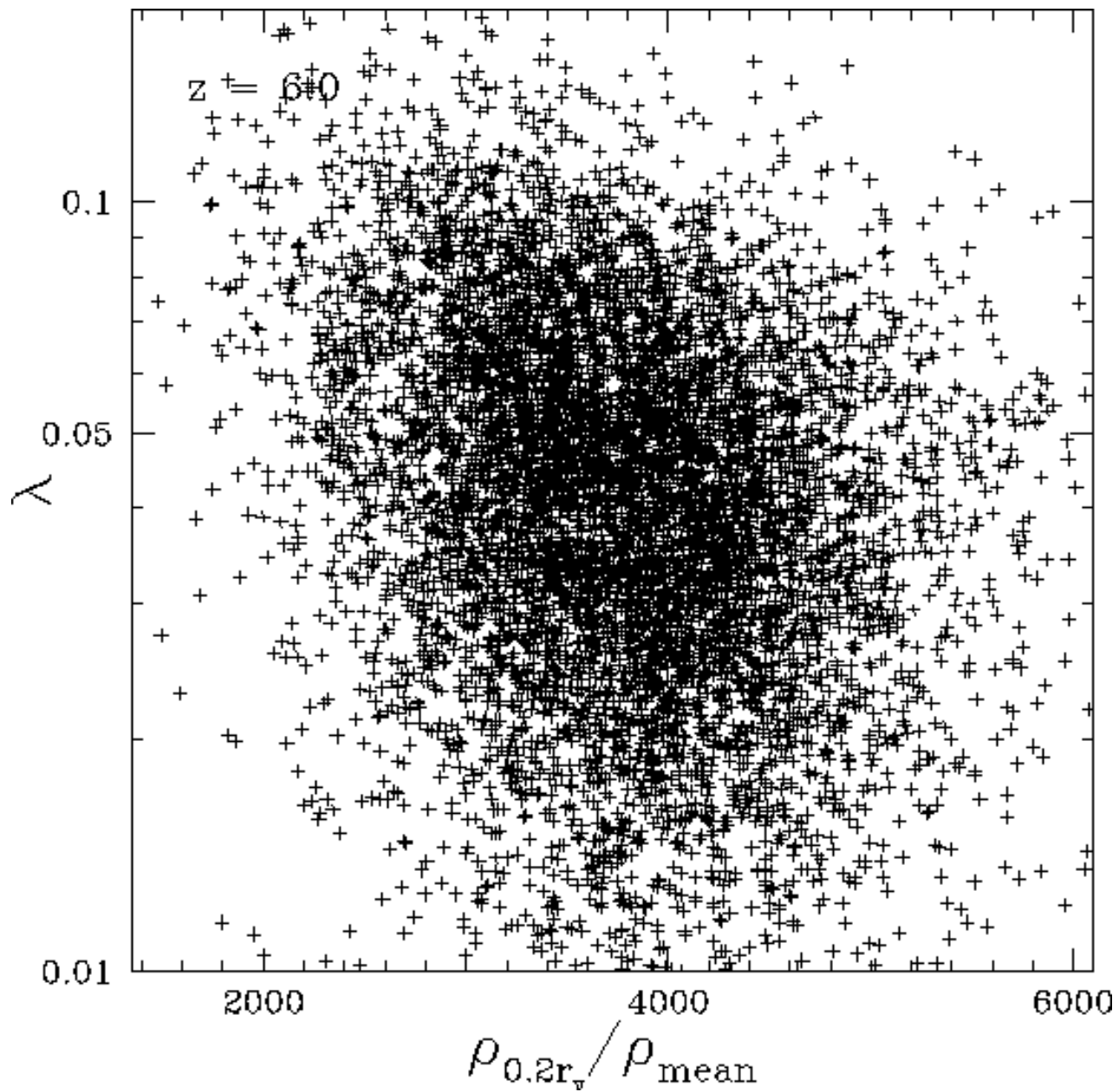


Fig. 16.— A scatter plot of the spin parameter, λ , versus the halo central density, defined as the density at $r < 0.2r_v$, for all the halos with $M > 10^6 h^{-1}M_\odot$ at $z = 6$.

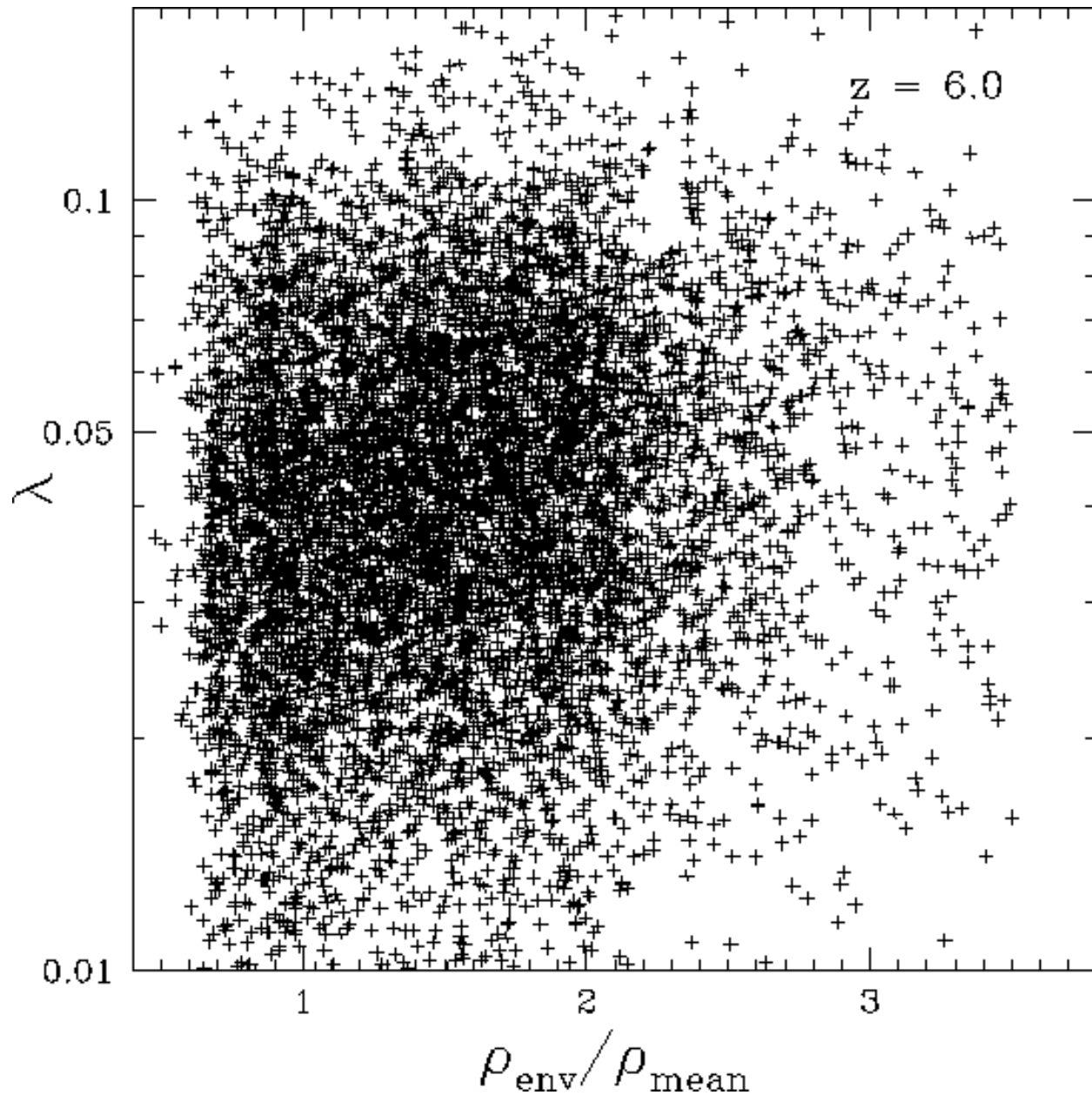


Fig. 17.— A scatter plot of the spin parameter, λ , versus the environmental density, defined as the dark matter density smoothed by a gaussian window of radius $0.3h^{-1}\text{Mpc}$, for all the halos with $M > 10^6 h^{-1}M_{\odot}$ at $z = 6$.

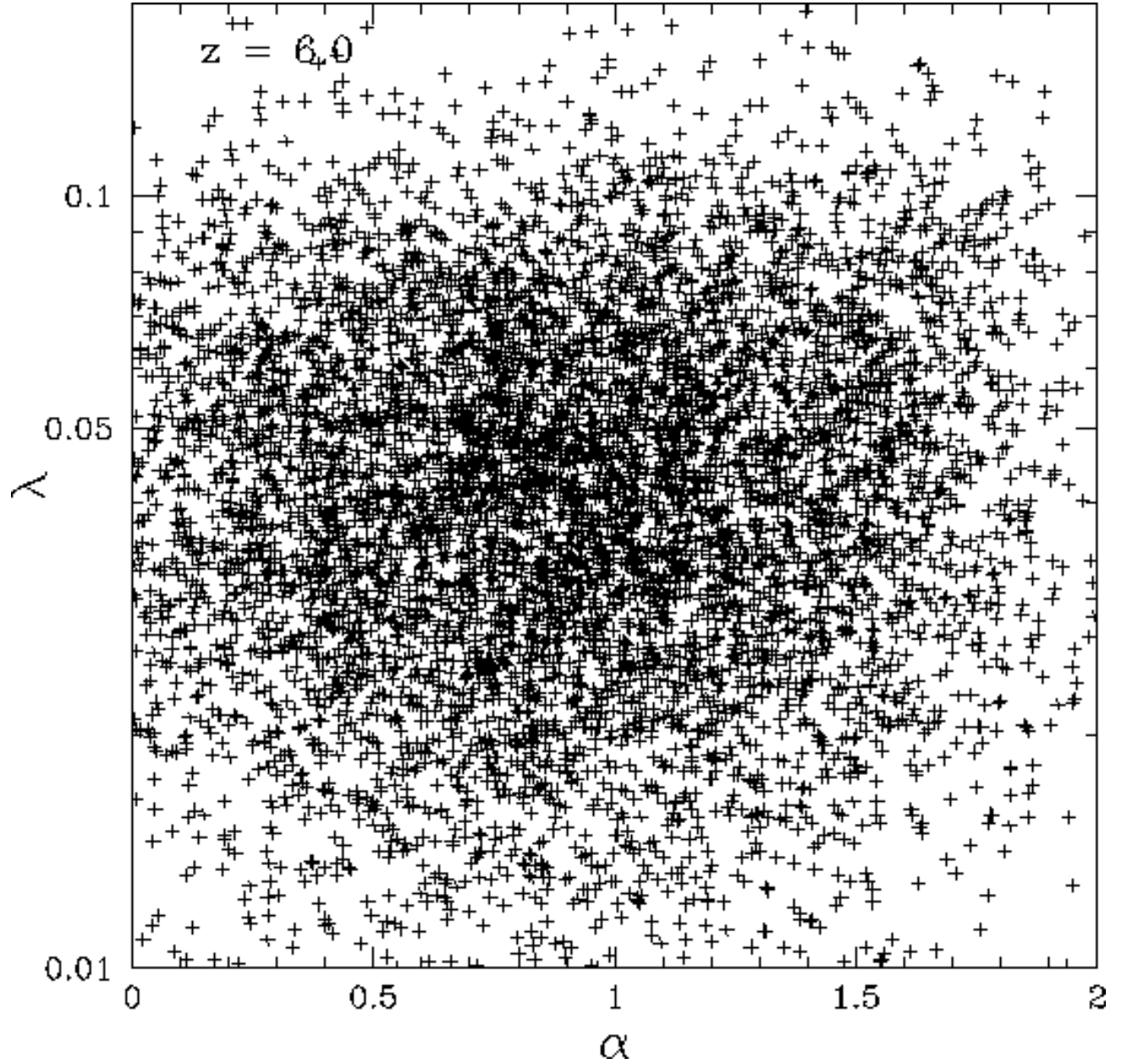


Fig. 18.— Comparison of the halo density profile slope parameter α versus spin parameter λ . No correlation between the two is observed.

Table 8. Spin Parameter : $\lambda_{median}(M,z)$

Halo Mass ($h^{-1} M_{\odot}$)	z=6.0	z=7.4	z=9.08	z=11.096
$10^{7.00} - 10^{7.25}$	0.043 ± 0.001	0.043 ± 0.001	0.042 ± 0.001	0.040 ± 0.001
$10^{7.25} - 10^{7.50}$	0.042 ± 0.001	0.041 ± 0.001	0.037 ± 0.001	0.037 ± 0.001
$10^{7.50} - 10^{8.00}$	0.041 ± 0.001	0.039 ± 0.001	0.035 ± 0.001	0.035 ± 0.002
$> 10^{8.00}$	0.035 ± 0.001	0.033 ± 0.001	0.031 ± 0.002	0.031 ± 0.007

Table 9. Spin Parameter : $\sigma_{\lambda}(M,z)$

Halo Mass ($h^{-1} M_{\odot}$)	z=6.0	z=7.4	z=9.08	z=11.096
$10^{7.00} - 10^{7.25}$	0.43 ± 0.01	0.44 ± 0.01	0.44 ± 0.01	0.41 ± 0.01
$10^{7.25} - 10^{7.50}$	0.43 ± 0.01	0.42 ± 0.01	0.38 ± 0.01	0.41 ± 0.02
$10^{7.50} - 10^{8.00}$	0.42 ± 0.01	0.41 ± 0.01	0.41 ± 0.01	0.32 ± 0.03
$> 10^{8.00}$	0.40 ± 0.01	0.39 ± 0.02	0.31 ± 0.04	0.43 ± 0.15

Table 10. Angular Momentum Profile : $A_0(M,z)$

Halo Mass ($h^{-1} M_{\odot}$)	z=6.0	z=7.4	z=9.08	z=11.096
$10^{7.0} - 10^{7.5}$	0.51 ± 0.03	0.49 ± 0.04	0.44 ± 0.06	0.44 ± 0.08
$10^{7.5} - 10^{8.0}$	0.55 ± 0.06	0.52 ± 0.12	0.48 ± 0.14	0.50 ± 0.16
$> 10^{8.0}$	0.56 ± 0.09	0.51 ± 0.21	0.49 ± 0.24	0.45 ± 0.32

Table 11. Angular Momentum Profile : $\sigma_A(M,z)$

Halo Mass ($h^{-1} M_{\odot}$)	z=6.0	z=7.4	z=9.08	z=11.096
$10^{7.0} - 10^{7.5}$	0.27 ± 0.03	0.28 ± 0.04	0.27 ± 0.06	0.25 ± 0.07
$10^{7.5} - 10^{8.0}$	0.26 ± 0.05	0.29 ± 0.10	0.29 ± 0.11	0.26 ± 0.12
$> 10^{8.0}$	0.27 ± 0.08	0.35 ± 0.18	0.29 ± 0.16	0.36 ± 0.23

the dark matter halo; all quantities are computed within the virial radius. We fit the λ distributions using a modified lognormal function:

$$P(\lambda) = \frac{1}{(\lambda + \epsilon_0)\sqrt{2\pi}\sigma_\lambda} \exp\left(-\frac{[\ln(\lambda + \epsilon_0) - \ln \lambda_0]^2}{2\sigma_\lambda}\right), \quad (8)$$

where ϵ_0 is fixed to be 0.0125, which is determined through experimentation. The modified lognormal fits for λ are shown as smooth curves in Figure 15; the goodness of the fits is typical. Tables 8,9 lists fitting parameters λ_0 and σ_λ , respectively. Note that the median value of λ is $\lambda_{med} = \lambda_0 - \epsilon_0$.

We see that the typical spin parameter has a value 0.03–0.04. However, the distribution of the spin parameter among halos is very broad, with a lognormal dispersion of ~ 0.4 . This implies that consequences that depend on the spin of a halo are likely to be widely distributed even at a fixed dark matter halo mass. Such consequences may include the size of a galactic disk and correlations between dark matter halo spin (conceivable misalignment between spin of gas and spin of dark matter would complicate the situation) and other quantities.

In Figures 16 and 17 we show the correlation between λ and the central density of the halo, and between λ and the environmental density, respectively. We find that there may possibly exist a weak correlations between λ and the central density of the halo, in the sense that halos with higher central densities (or equivalently earlier formation times) have lower λ , with a very large scatter, whereas no correlation is discernible between λ and the environmental density. Finally, Figure 18 show the relation between λ and α , where no correlation is visible.

3.6. Angular Momentum Profile For Dark Matter Halos

Next, we compute the angular momentum profiles for individual dark matter halos. We then fit the each angular momentum profile by the following function in the small $|j|$ regime:

$$\frac{M(< j)}{M_v} = A \frac{j}{j_0} + \frac{M(< 0)}{M_v}, \quad (9)$$

where A and $M(< 0)$ are two fitting parameters; M_v is the virial mass and $j_0 \equiv J/M_v = \lambda GM^{3/2}/|E|^{1/2}$.

In order to compute the angular momentum profile an appropriate smoothing window needs to be applied to dark matter particles. We find that $M(< 0)/M_v$ varies for different smoothing scales, with typical values around 0.2, while A remains roughly constant for each individual halo. However, A is broadly distributed for all dark matter halos. Figure 19

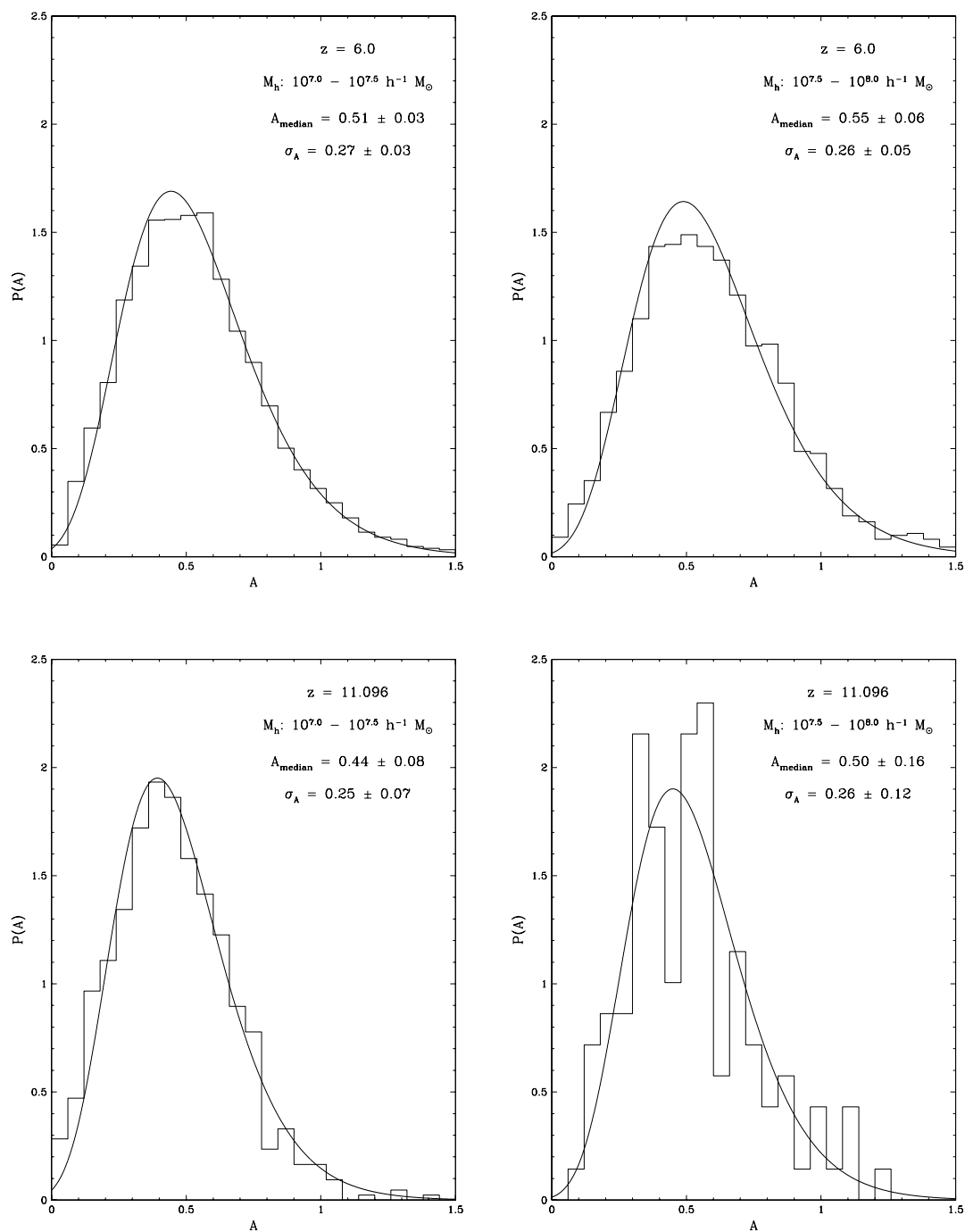


Fig. 19.— The distributions of slope parameter A in the halo angular momentum profile fitting for four randomly selected cases upon different mass and redshift. The lognormal fits are shown as smooth curves.

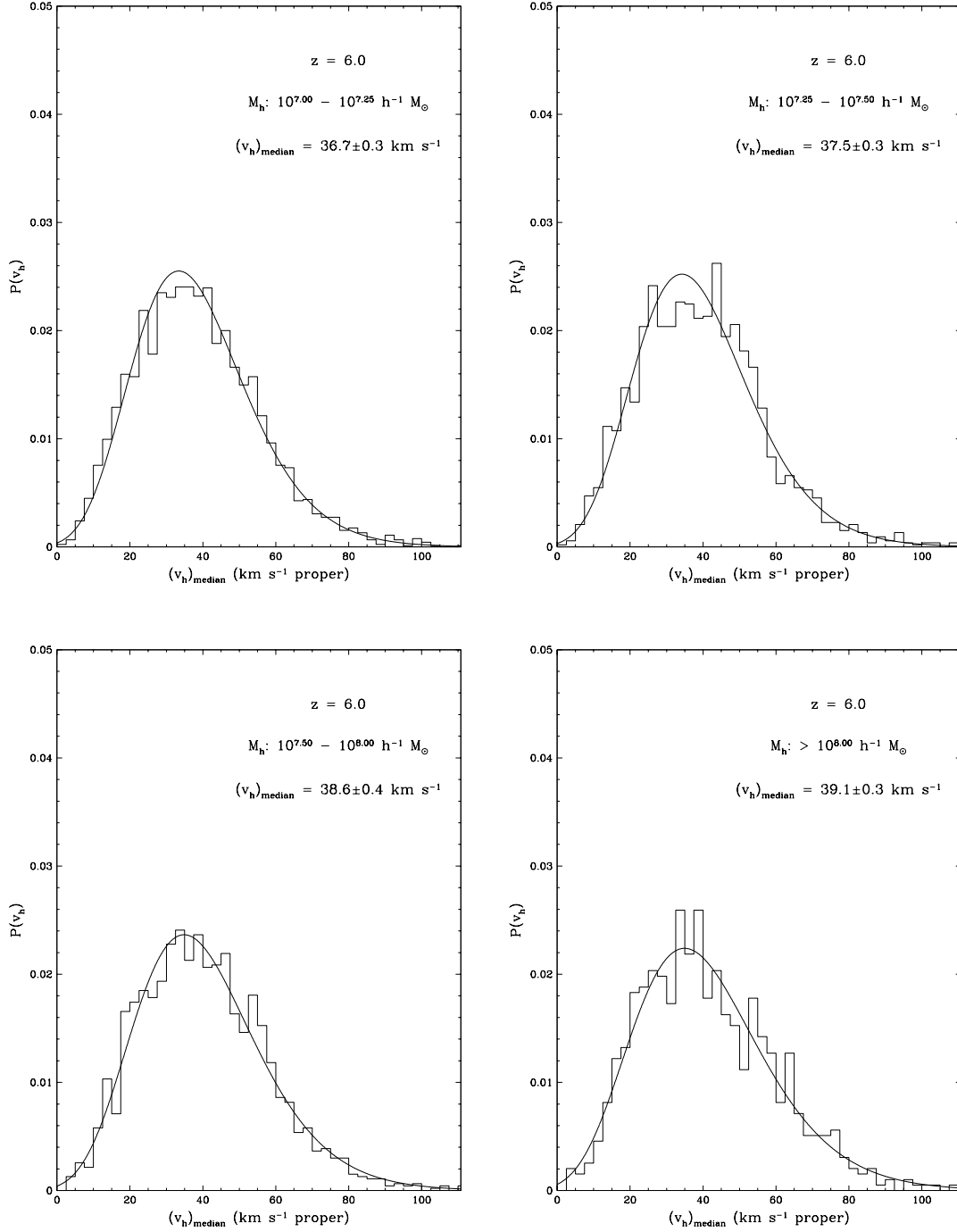


Fig. 20.— The distributions of dark matter halo peculiar velocity for four mass bins at $z = 6$. The lognormal fits are shown as smooth curves.

show histograms for the distributions of A_0 , for four randomly selected cases. We fit the A distribution using a modified lognormal function:

$$P(A) = \frac{1}{(A + \epsilon_A)\sqrt{2\pi}\sigma_A} \exp\left(-\frac{[\ln(A + \epsilon_A) - \ln A_0]^2}{2\sigma_A^2}\right), \quad (10)$$

where $\epsilon_A = 0.4$ is fixed through experimentation. Tables 10,11 list fitting parameters A_0 and σ_A , respectively.

In general we find our fitting formula (Equation 10) provides a good fit for each individual halo. The distribution of matter at small j is most relevant for the formation of central objects, such as black holes (e.g., Colgate et al. 2003) or bulges (e.g., D’Onghia & Burkert 2004). Our calculation indicates that the fraction of mass in a halo having specific angular momentum less than a certain value is roughly 0.5 times the ratio of that value over the average specific angular momentum of the halo.

3.7. Bulk Velocity of Dark Matter Halos

Finally, we compute the peculiar velocity of dark matter halos. We find that the distribution once again can be fitted by lognormal distributions as equation (9). In order to provide a good fit for the results at $z = 6$ shown in Figure 20, it is found that $\epsilon = 40\text{km/s}$ in equation (8) with median velocity $v_m \sim 38 \pm 2\text{km/s}$ and lognormal dispersion $\sigma_v = 0.22 \pm 0.01$. We caution, however, the absolute value of the peculiar velocity of each halo, unlike the quantities examined in previous subsections, may be significantly affected by large waves not present in our simulation box. Adding missing large waves should increase the zero point ϵ to a larger value. Therefore, the peculiar velocity shown should be treated as a lower limit. In other words, expected peculiar velocity of dark matter halos at these redshifts are likely in excess of $30 - 40\text{km/s}$.

4. Conclusions

Using a high resolution TPM N-body simulation of the standard cold dark matter cosmological model with a particle mass of $m_p = 3.57 \times 10^4 h^{-1}M_\odot$ and a softening length of $\epsilon = 0.14 h^{-1}\text{kpc}$ in a $4h^{-1}\text{Mpc}$ box, we compute various properties of dark matter halos with mass $10^{6.5} - 10^9 M_\odot$ at redshift $z = 6 - 11$. We find the following results.

- (1) Dark matter halos at such small mass at high redshifts are already significantly biased over matter with a bias factor in the range $2 - 6$.

- (2) The dark matter halo mass function displays a slope at the small end 2.05 ± 0.15 .
- (3) The central density profile of dark matter halos are found to be in the range $(0.4 - 1.0)$ well fitted by $\alpha_0 = 0.75((1+z)/7.0)^{-1.25}(M/10^7 M_\odot)^{0.11(1+z)/7.0}$ with a dispersion of ± 0.5 , in rough agreement with the theoretical arguments given in Ricotti (2003) and Subramanian et al. (2000).
- (4) The median spin parameter of the dark matter halos is $0.03 - 0.04$ but with a lognormal dispersion of ~ 0.4 . The angular momentum profile at the small end is approximately linear with the fraction of mass in a halo having specific angular momentum less than a certain value is roughly 0.5 times the ratio of that value over the average specific angular momentum of the halo.
- (5) The dark matter halos move at a typical velocity in excess of $30 - 40$ km/s.

This research was supported in part by AST-0206299 and NAG5-13381. The computations were performed on the National Science Foundation Terascale Computing System at the Pittsburgh Supercomputing Center.

REFERENCES

- Becker, R.H., et al. 2001, AJ, 122, 2850
- Bertschinger, E., & Gelb, J.M. 1991, Computers in Physics, 5, 164
- Bertschinger, E. 2001, ApJS, 137, 1
- Bode, P., & Ostriker, J.P. 2003, ApJS, 145, 1
- Bode, P., Ostriker, J.P., & Xu, G. 2000, ApJS, 128, 561
- Cen, R. 2003, ApJ, 591, 12
- Colgate, S.A., Cen, R., Li, H., Currier, N., & Warren, M.S. 2003, ApJL in press, astro-ph/0310776
- D’Onghia, E., & Burkert, A. 2004, astro-ph/0402504
- Fan, X., et al. 2001, AJ, 122, 2833
- Lacey, C., & Cole, S. 1993, MNRAS, 262, 627.
- Ma, C.-P., & Bertschinger, E. 1995, ApJ, 455, 7
- Mo, H.J., & White, S.D.M. 1996, MNRAS, 282, 347
- Navarro, J., Frenk, C.S., & White, S.D.M. 1997, ApJ, 490, 493

Peebles, P.J.E. 1969, ApJ, 155, 393

Press, W.H., & Schechter, P. 1974, ApJ, 187, 425

Peebles, P.J.E. 1993, Principles of Physical Cosmology (Princeton: Princeton University Press)

Ricotti, M. 2003, MNRAS, 344, 1237

Syer, D., & White, S.D.M. 1998, MNRAS, 293, 337

Subramanian, K., Cen, R., & Ostriker, J.P. 2000, ApJ, 538, 528

Xu, G. 1995, ApJS, 98, 355